

Polarized Reflectance and Transmittance Properties of Wind-blown Sea Surfaces

Curtis D. Mobley¹

¹*Sequoia Scientific, Inc., 2700 Richards Road,
Suite 107, Bellevue, Washington 98005, USA*

compiled: January 27, 2015

Generation of random sea surfaces using wave variance spectra and Fourier transforms is formulated so that wave energy is conserved and both wave height and slope variance are fully resolved. Monte Carlo polarized ray tracing that accounts for multiple scattering between light rays and wave facets is used to compute effective Mueller matrices for reflection and transmission of air- or water-incident polarized radiance. Irradiance reflectances computed using a Rayleigh sky radiance distribution, sea surfaces generated with Cox-Munk statistics, and unpolarized ray tracing are in error by 10-18% compared to values computed using elevation- and slope-resolving surfaces and polarized ray tracing. Radiance reflectance factors as used to estimate water-leaving radiance from measured upwelling and sky radiances are shown to depend on sky polarization, and improved values are given.

OCIS codes: (010.4450) Oceanic optics; (260.5430) Polarization; (290.5855) Scattering, polarization; (010.0280) Remote sensing and sensors.

<http://dx.doi.org/10.1364/XX.99.099999>

1. Introduction

Optical reflection and transmission by water surfaces are fundamental to radiative transfer calculations for oceanic and atmospheric applications. Reflection of sun and sky radiance by the sea surface creates glint. In ocean color remote sensing of water-column conditions, glint is an undesired contribution to the measured upwelling radiance that, along with atmospheric path radiance, must be estimated and removed from the measured radiance in order to obtain the water-leaving radiance, which carries the information about the water column itself. In remote sensing of the surface wave state or wind speed and direction, glint is the signal because it depends on surface roughness. The water-leaving radiance itself comes from upwelling underwater radiance that is transmitted through the sea surface from water to air. The underwater light field arises from light that is transmitted through the surface from air to water and is affected by underwater radiance that is reflected back downward by the un-

derside of the sea surface.

There are three requirements for accurate calculation of surface optical properties. First, the sea surface itself must be modeled in a way that accounts for both wave elevation and slope. To first order, reflection and transmission of a light ray incident onto the sea surface are governed by the slope of the surface at the point of intersection. However, wave elevation can lead to wave shadowing for incident angles near the horizon, which refers to rays predominately striking the sides of the waves tilted toward the light source. In the ocean, wave elevation is dominated by the highest amplitude waves, which are generally gravity waves with wavelengths of tens to hundreds of meters. The waves with the largest slopes are often gravity waves with wavelengths of a meter or less and capillary waves, whose wavelengths are a few millimeters. Thus the simulated sea surface must include the elevation and slope effects for spatial scales that vary by a factor of 10^5 .

Second, the simulated light rays must account for polarization. Surface reflection and transmission induce polarization even if the incident source (e.g., the sun's direct beam) is unpolarized. Incident sky radiance is usually partially linearly polarized. Thus both reflected and transmitted light fields are in general partially polarized. Although many sensors are designed to be insensitive to polarization, the state of polarization of the incident light affects the total energy reflected or transmitted by the sea surface. Polarization also carries information that potentially can be used to improve algorithms for removal of surface glint, underwater visibility, or separation of particle types, if polarization-sensitive sensors are employed.

Third, the ray tracing must account for multiple scattering between light rays and waves. Although single scattering dominates ray-surface interactions, multiple scattering can occur for incident angles that are large relative to the local normal to the sea surface. This occurs most often when the incident ray is nearly horizontal, e.g. when the sun is near the horizon.

Simulations of sea surfaces for optical calculations often employ the Cox-Munk wind speed-wave slope statistics for generation of random surface realizations. Their equations [1]

$$\sigma_a^2 = 0.0316U_{12.5} \quad (1a)$$

$$\sigma_c^2 = 0.0192U_{12.5} \quad (1b)$$

relate the along-wind (σ_a^2) and cross-wind(σ_c^2) variances of the sea surface slopes to the wind speed $U_{12.5}$ in meters per second at 12.5 m above sea level. Surfaces generated using these equations capture slope effects for the full range of wave spatial scales because the equations are based on observations of well developed seas. Preisendorfer and Mobley [2] used Cox-Munk surfaces and a ray tracing algorithm that included all orders of multiple scattering to study sea surface optical properties, but only for unpolarized light. Although the Cox-Munk model provides a reasonable simulation of surface slopes for fully developed seas, it cannot reproduce wave elevations.

Both elevation and slope statistics can be captured if wave variance spectra and Fourier transforms are used for surface generation. These surfaces are referred to here as FFT surfaces because the fast Fourier transform (FFT) is used to evaluate the discrete Fourier transforms. Several previous studies [3–7] have used FFT surfaces, but have not included polarization or multiple scattering. Tulldahl and Steinval [8] used a two-step, two-

scale model to simulate the effects of both gravity and capillary waves on wave slopes. In the first step of their calculations, they used a coarse spatial grid to resolve the gravity waves. In the second step, they added capillary-scale waves to the coarse grid. Their capillary-scale waves were generated using slope variances equal to the difference of the Cox-Munk slope variance and the slope variance of the gravity waves generated in the first step. Their surfaces thus accounted for slope effects due to the full range of wavelengths, and their ray tracing used the same multiple scattering algorithm as [2]. They did not, however, include polarization. McLean [5] accounted for unresolved slope variance in a study of lidar transmission through the surface by adding extra divergence to the lidar beam when it passed through the sea surface. A later similar study [6] used a grid resolution of 0.5 cm to capture the slopes of capillary-scale waves, but the longest gravity waves were not fully resolved. The recent study by Kay et al. [7] simulated the full range of spatial scales from 200 m to 3 mm needed to resolve the amplitude and slope variances, but their brute-force computations required 65536×65536 grid points in the FFTs, with consequently very slow run times of 6 hours to generate a single surface realization. They also did not include polarization.

The previous studies just cited have thus included at best two of the three above-mentioned requirements for accurate computation of sea surface optical properties. The first goal of the present paper is to present techniques for computing optical properties for sea surfaces that incorporate both elevation and slope effects for the full range of gravity and capillary spatial scales, with all orders of multiple scattering between light rays and surface waves, and including polarization via the full Stokes vector formalism. The second goal is to compare predictions made with the complete formalism with those made using the simplifications of Cox-Munk surfaces, unpolarized ray tracing, and/or single scattering. Fortran 95 code was written to implement the surface-generation and ray-tracing algorithms described in the next two sections. That code can generate either Cox-Munk or FFT surfaces, and the ray tracing can be either polarized or unpolarized. The ray tracing keeps a separate tally for singly and multiply scattered rays. It is thus easy to compare results obtained for different sea surface models, for polarized vs. unpolarized treatments of the light, and for single vs. multiple scattering.

The next section describes the surface wave gen-

eration, including an algorithm to account for elevation and slope variances without the need for large numbers of grid points. The polarized ray-tracing algorithm is outlined in the following section. Section 4 then shows examples of reflectance and transmittance for both water- and air-incident light for the simple case of an unpolarized, collimated incident beam. Reflection and transmission of a polarized Rayleigh sky radiance distribution are then illustrated in Section 5. Section 6 then compares exact calculations (i.e., using FFT surfaces and polarized ray tracing with multiple scattering) of sea surface irradiance reflectance with results obtained using various approximations. The use of radiance reflectance factors for surface glint removal is well established [9]. The final Section 7 compares these factors as computed using FFT surfaces and polarized ray tracing with the factors obtained with Cox-Munk surfaces and unpolarized ray tracing.

2. Sea Surface Generation

The initial part of this section reviews the relations between sea surfaces and the wave elevation and slope variance spectra needed for sea surface generation. The next part then shows how a wave variance spectrum is used to define random sea surfaces that are consistent with the chosen wave spectrum. Particular attention is paid to the normalization factors that are required for conservation of wave elevation variance (proportional to wave energy) in a round-trip calculation from a wave variance spectrum to a sea surface realization and back to a wave spectrum. The final section shows how a wave elevation variance spectrum can be re-scaled so that a finite range of sampling of the spectrum in frequency space generates sea surfaces that reproduce the elevation and slope statistics of the real sea surface corresponding to the original variance spectrum.

2.A. Wave Variance Spectra

The Monte Carlo ray tracing begins with the generation of random realizations of sea surfaces. Let $z(\mathbf{x}) = z(x, y)$ be the sea surface elevation in meters at point $\mathbf{x} = (x, y)$ at a particular time. The spatial extent of the sea surface is $0 \leq x < L_x$ and $0 \leq y < L_y$, with L_x and L_y in meters. A wind-centered coordinate system is used, with the $+x$ direction chosen to be downwind; $-x$ is then upwind, and $\pm y$ are the cross-wind directions. This surface is sampled on a rectangular grid of N_x by N_y points, where both N_x and N_y are powers of 2 to enable use of FFTs. The spatial sampling points are then $x(r) = r\Delta x, r = 0, \dots, N_x - 1$ with $\Delta x = L_x/N_x$. A

similar equation holds for the $y(s) = s\Delta y$ points. A discrete sample of $z(x, y)$ is denoted $z(\mathbf{x}_{rs})$ or $z(r, s)$.

The two-dimensional (2D) forward discrete Fourier transform of $z(r, s)$, which is evaluated using the FFT algorithm, converts the surface elevations to a 2D grid of complex Fourier amplitudes $\hat{z}(u, v) = FFT_{2D}\{z(r, s)\}$. These amplitudes are defined at positive and negative discrete angular spatial frequencies $k_x(u) = u\Delta k_x, u = -(N_x/2 - 1), \dots, N_x/2$, with $\Delta k_x = 2\pi/L_x$. The fundamental frequency of magnitude Δk_x corresponds to the longest resolvable wave. The positive frequency $k_x(N_x/2) = 2\pi/(2\Delta x)$ is the Nyquist frequency, which corresponds to the shortest resolvable wavelength of $2\Delta x$. Corresponding results hold for the $k_y(v)$ spatial frequencies. These spatial frequencies have units of rad/m. A discrete frequency pair $\mathbf{k}_{uv} = [k_x(u), k_y(v)]$ is labeled by (u, v) . The sea surface $z(\mathbf{x}_{rs})$ is real valued, so the amplitudes are Hermitian: $\hat{z}^*(-\mathbf{k}_{uv}) = \hat{z}(+\mathbf{k}_{uv})$, where \hat{z}^* denotes the complex conjugate of \hat{z} .

The absolute value squared of the discrete amplitudes is the discrete elevation variance spectrum corresponding to the surface sample $z(r, s)$. This spectrum is denoted $\Psi(u, v) = |\hat{z}(u, v)|^2$. Dividing the discrete spectrum by the sampling bandwidth gives an estimate (a periodogram) of the continuous elevation variance spectral density: $\Psi(k_x, k_y) = \Psi(u, v)/(\Delta k_x \Delta k_y)$. Averaging the periodograms from many independent samples of the sea surface averages out the statistical noise inherent in each individual periodogram and leads to the elevation spectral density of the sea surface. It is important to note that the discrete $z^2(r, s)$, $|\hat{z}(u, v)|^2$, and $\Psi(u, v)$ are all point functions with units of m², whereas the continuous function $\Psi(k_x, k_y)$ is a spectral density with units of m²/(rad/m)². Moreover, the integral of $\Psi(k_x, k_y)$ over all spatial frequencies gives the variance of the zero-mean sea surface elevation:

$$var\{z\} = \langle z^2 \rangle = \int_{-\infty}^{\infty} \int_{-\infty}^{\infty} \Psi(k_x, k_y) dk_x dk_y,$$

where $\langle \rangle$ indicates expectation or ensemble average over many measurements of the sea surface. The energy contained in a surface wave is proportional to the wave amplitude squared, so variance spectra are often loosely called energy spectra, and conservation of wave energy corresponds to conservation of elevation variance.

The FFT of $z(r, s)$ returns a discrete two-sided (2S) spectrum, denoted by $\Psi_{2S}(\mathbf{k}_{uv})$. “Two-sided”

means that both positive and negative frequencies, which correspond to waves propagating in opposite directions, are present. With the choice of $+x$ being downwind, frequencies with a positive k_x value correspond to waves propagating generally downwind ($|\varphi| < \pi/2$, where $\varphi = \tan(k_y/k_x)$); negative k_x corresponds to waves propagating upwind ($|\varphi| > \pi/2$).

The resulting $\Psi_{2S}(\mathbf{k}) = \Psi_{2S}(k_x, k_y)$ is equal for directions $+\mathbf{k}$ and $-\mathbf{k}$. This symmetry arises because the FFT cannot determine which direction a wave is propagating because there is no time dependence in the surface sample $z(r, s)$. In many applications in physical oceanography, the quantity of interest is just the total variance (i.e., total energy) per unit frequency interval contained in waves of a given frequency magnitude $k = |\mathbf{k}| = (k_x^2 + k_y^2)^{1/2}$, without regard for the direction of wave propagation. In this case, a one-sided (1S) spectral density is used, which has only positive k values but is twice the magnitude of the two-sided spectrum: $\Psi_{1S}(k) = 2\Psi_{2S}(k)$. Wave spectral densities as presented in the oceanographic literature are invariably one-sided spectra. However, when generating sea surfaces as described below, two-sided spectra are needed, in which case the one-sided spectrum must be divided by two to convert it back to the proper magnitude of a two-sided spectrum. In reality, $\Psi_{2S}(\mathbf{k}) \gg \Psi_{2S}(-\mathbf{k})$ because much more energy propagates downwind than upwind at a given frequency, but symmetric spectra are consistent with the generation of time-independent surfaces as needed for the present study.

This study uses the one-sided elevation variance spectral density of Elfouhaily et al. [10], which they write in polar coordinates (k, φ) as

$$\Psi_{1S}(k, \varphi) = \frac{1}{k} \mathcal{S}(k) \Phi(k, \varphi).$$

Here $\mathcal{S}(k)$ is the 1D omnidirectional spectral density with units of $\text{m}^2/(\text{rad}/\text{m})$, and $\Phi(k, \varphi)$ is a non-dimensional spreading function. $\Psi_{1S}(k, \varphi)$ thus has the same units as $\Psi_{1S}(k_x, k_y)$. Their spreading function has the form

$$\Phi(k, \varphi) = \frac{1}{2\pi} [1 + \Delta(k) \cos(2\varphi)]. \quad (2)$$

This function is symmetric about $\varphi = \pm\pi/2$; i.e., the function gives symmetric spreading for both downwind and upwind propagation.

The Ψ spectra give the variance of the sea surface elevations. The corresponding variance spectrum of the sea surface slopes is $k^2 \Psi$. Thus the variance

of the wave slopes (the mean square slope) in the along-wind ($\pm x$) direction is given by either of

$$\begin{aligned} \sigma_a^2 &= \int_{-\infty}^{\infty} \int_{-\infty}^{\infty} k_x^2 \Psi_{2S}(k_x, k_y) dk_x dk_y \\ &= \int_0^{\infty} \int_{-\pi}^{\pi} k^2 \cos^2 \varphi \Psi_{2S}(k, \varphi) k dk d\varphi. \end{aligned}$$

A similar equation gives the cross-wind slope variance. The total slope variance is then $\sigma^2 = \sigma_a^2 + \sigma_c^2 = \int_0^{\infty} k^2 \mathcal{S}(k) dk$. Wave spectra are discussed in detail in [11, Appendix A].

2.B. Surface Generation via FFTs

The next task is to generate a set of random discrete complex Fourier amplitudes that are physically consistent with the chosen wave elevation variance spectrum. These amplitudes must be defined for both positive and negative frequencies, and they must be Hermitian so that the inverse Fourier transform generates a real sea surface. In essence, the elevation variance spectrum is used to define the wave amplitudes as a function of spatial frequency, and random variables are used to define a random phase for each wave.

Following the formulation of Tessendorf [12] first define

$$\hat{z}_o(\mathbf{k}_{uv}) \equiv \frac{1}{\sqrt{2}} [\rho(\mathbf{k}_{uv}) + i\sigma(\mathbf{k}_{uv})] \times \left[\frac{\Psi_{1S}(\mathbf{k} = \mathbf{k}_{uv})}{2} \Delta k_x \Delta k_y \right]^{1/2} \quad (3)$$

$$= \frac{1}{\sqrt{2}} [\rho(\mathbf{k}_{uv}) + i\sigma(\mathbf{k}_{uv})] \sqrt{\Psi_{2S}(\mathbf{k}_{uv})}. \quad (4)$$

Here $\rho(\mathbf{k}_{uv})$ and $\sigma(\mathbf{k}_{uv})$ are independent normal random variables with zero mean and unit variance, denoted $\mathcal{N}(0, 1)$. A different random variable is drawn for each \mathbf{k}_{uv} value. $\Psi_{1S}(\mathbf{k} = \mathbf{k}_{uv})$ is a one-sided continuous spectral density evaluated at the discrete frequencies \mathbf{k}_{uv} . Note in Eq. (3) that the one-sided spectrum is divided by 2 in the process of generating the symmetric discrete two-sided spectrum of Eq. (4). This division by two reflects the assumption that the one-sided spectrum corresponds to a symmetric two-sided spectrum. Multiplication of the continuous spectral density by the sampling frequency bandwidths converts the spectral density to a discrete point function showing how much variance is contained in a finite frequency interval $\Delta k_x \Delta k_y$ at each frequency \mathbf{k}_{uv} . $\Psi_{2S}(\mathbf{k}_{uv})$ denotes the resulting two-sided, discrete variance spectrum.

The amplitudes $\hat{z}_o(\mathbf{k}_{uv}) = \hat{z}_o(u, v)$ are random variables. The statistical expectation of $|\hat{z}_o(\mathbf{k}_{uv})|^2$ is

$$\begin{aligned} & \langle \hat{z}_o(u, v) \hat{z}_o^*(u, v) \rangle \\ &= \left\langle \left\{ \frac{1}{\sqrt{2}} [\rho(u, v) + i\sigma(u, v)] \sqrt{\Psi_{2S}(u, v)} \right\} \times \right. \\ & \quad \left. \left\{ \frac{1}{\sqrt{2}} [\rho(u, v) - i\sigma(u, v)] \sqrt{\Psi_{2S}(u, v)} \right\} \right\rangle \\ &= \frac{\Psi_{2S}(u, v)}{2} [\langle \rho^2(u, v) \rangle + \langle \sigma^2(u, v) \rangle] \\ &= \Psi_{2S}(u, v), \end{aligned}$$

where it has been noted that $\langle \rho^2(u, v) \rangle = \langle \sigma^2(u, v) \rangle = 1$ for independent $\mathcal{N}(0, 1)$ random variables. Thus $\hat{z}_o(u, v)$ is consistent with the chosen variance spectrum. However, $\hat{z}_o(u, v)$ is not Hermitian, so the inverse FFT would not give a real sea surface.

However, the spectral amplitudes defined by

$$\hat{z}(\mathbf{k}_{uv}, t) \equiv \frac{1}{\sqrt{2}} [\hat{z}_o(+\mathbf{k}_{uv}) \exp(-i\omega_{uv}t) + \hat{z}_o^*(-\mathbf{k}_{uv}) \exp(+i\omega_{uv}t)] \quad (5)$$

are clearly Hermitian, so the inverse FFT applied to $\hat{z}(\mathbf{k}_{uv}, t)$ will give a real-valued $z(\mathbf{x}_{rs}, t)$. Time dependence is included in this definition for complete generality. Just as was done for $\langle |\hat{z}_o(\mathbf{k}_{uv})|^2 \rangle$ above, it is easy to show that $\langle |\hat{z}(\mathbf{k}_{uv}, t)|^2 \rangle = \frac{1}{2} [\Psi_{2S}(\mathbf{k}_{uv}) + \Psi_{2S}(-\mathbf{k}_{uv})]$. Thus the amplitudes of Eq. (5) give a real sea surface that is consistent with the chosen energy spectrum. This result holds even if the two-sided spectrum is not symmetric for $\pm\mathbf{k}$. The time independence of the expectation shows that even though the shape of the wave surface depends on time, the total energy of the wave field does not.

If a sequence of independent surfaces is to be generated, as needed for the Monte Carlo simulations below, then the time can be set to 0 in Eq. (5). Each surface is then generated by drawing a new set of random numbers in Eq. (4). If the time-dependent propagation of a given surface is to be simulated, e.g. for creating a visual rendering of moving waves, then a single set of random numbers is drawn, and the time dependence is obtained from the exponentials of Eq. (5) and an appropriate dispersion relation to obtain the temporal angular frequency ω_{uv} from the spatial angular frequency k_{uv} . For deep-water gravity waves, the dispersion relation is $\omega_{uv}^2 = gk_{uv}$, where g is the acceleration due to gravity. Note, however, that when generating a time-dependent sequence of surfaces for a

propagating wave field, it is necessary to use an asymmetric spreading function so that most of the energy propagates downwind. A commonly used spreading function for this purpose is the cosine-2s family [13] of the form $\Phi(k, \varphi) = C(s) \cos^{2s}(\varphi/2)$, where s is a spreading parameter that depends on k , and C is a normalization coefficient. These functions are asymmetric about $\varphi = \pi/2$ and give much stronger propagation downwind than upwind. In this case, essentially all of the variance is contained in the downwind half of $\Psi_{2S}(\mathbf{k})$, and no division by two is needed in Eq. (3). In any case, the random realization of the sea surface is obtained from the inverse FFT of the amplitudes: $z(r, s, t) = \text{FFT}_{2D}^{-1}\{\hat{z}(\mathbf{k}_{uv}, t)\}$.

Equations similar to (3) and (5) are widely used in the movie industry for computer-generated imagery of sea surfaces. However, the literature on those applications (e.g., [12]) always ignores the division of the one-sided variance spectrum by 2 as seen in Eq. (3), and the leading factor of $1/\sqrt{2}$ seen in Eq. (5) is likewise missing. Multiplication by the frequency interval as seen in Eq. (3) is also often ignored. The justification seems to be that scale factors do not matter because the generated surfaces subsequently will be distorted for artistic purposes, e.g. to make the waves appear larger. However, for scientific applications it is crucial that the generated sea surfaces be physically correct. When generating time-independent surfaces with a symmetric spreading function such as that of Eq. (2), if Ψ_{1S} is not divided by 2 in Eq. (3) and the $1/\sqrt{2}$ factor is omitted in Eq. (5), then the amplitudes will be a factor of two too large. This corresponds to a factor of four violation of conservation of variance (i.e. energy) in a round trip calculation from variance spectrum to sea surface and back to variance spectrum.

2.C. Accounting for Unsampled Variance

Generation of a sea surface requires specific values for L_x, L_y, N_x and N_y in the above equations. This raises the question of how large a spatial region and how many points must be used in generating sea surface realizations. Not surprisingly, the answer depends on the application. The visual impression of a sea surface is, to first order, determined by the height of the waves, which in turn is governed by the largest gravity waves for the given wind speed. When creating sea surfaces for rendering into a visually appealing movie scene, L_x and L_y can be chosen large enough to resolve the gravity waves with the greatest elevation variance (estimated from the

peak of the $\mathcal{S}(k)$ spectrum). The number of grid points can be small; $2^{10} = 1024$, $2^{11} = 2048$, or perhaps at most $2^{12} = 4096$ grid points in each direction are usually adequate.

Accurate scientific calculations of sea surface reflectance require many more grid points in order to resolve the surface down to the millimeter scale where capillary waves make a significant contribution to the surface slope variance. It is now computationally possible to create 2D FFT surfaces with sufficiently large N values in the x and y directions, but run times are prohibitive. Kay et al. [7] created 200 m by 200 m surfaces with $2^{16} = 65536$ points in each dimension. This allowed sampling of the variance spectrum for wavelengths from 200 m gravity waves to 3 mm capillary waves. However, it took 6 hours to create just one surface on a 3 GHz computer. Many ray tracing applications require tens to hundreds of thousands of independent surface realizations to obtain satisfactory statistical estimates. Thus it is necessary to finesse certain calculations so that large- N FFTs can be avoided.

The upper-left panel of Fig. 1 shows the omnidirectional elevation spectrum $\mathcal{S}(k)$ of Elfouhaily et al. [10] for a wind speed of 10 m s⁻¹. The upper-right panel shows the corresponding slope variance $k^2\mathcal{S}(k)$. Note that the slope spectrum falls off much more slowly with increasing k than does the elevation spectrum. The elevation and slope variances contained in these spectra can be computed by numerically integrating the spectra from some very low frequency k_0 to a very high frequency k_∞ , which cover the frequency range where the spectra are non-negligible in magnitude:

$$\langle z^2 \rangle = \int_{k_0}^{k_\infty} \mathcal{S}(k) dk, \quad (6)$$

and

$$\sigma^2 = \int_{k_0}^{k_\infty} k^2 \mathcal{S}(k) dk. \quad (7)$$

Using $k_0 = 0.01$ and $k_\infty = 10^4$ gives $\langle z^2 \rangle = 0.4296$ m² and $\sigma^2 = 0.06011$ rad² for the spectrum of the present example.

Now suppose this spectrum is used to generate a surface with $L_x = 200$ m using $N_x = 1024$ sampling points. The fundamental spatial frequency corresponding to the longest resolvable wavelength is then $k_f = 2\pi/L_x = 0.0314$ rad m⁻¹ and the Nyquist frequency is $k_{Ny} = 16.085$ rad m⁻¹; these frequencies are shown by the two red dots in the upper panels of Fig. 1. These two frequencies and the $N_x - 2$ evenly spaced frequencies in between

are the frequencies at which the elevation variance spectrum is sampled. Using k_f and k_{Ny} as the lower and upper limits in Eqs. (6) and (7) gives $\langle z^2 \rangle(N = 1024) = 0.4219$ m² and $\sigma^2(N = 1024) = 0.02584$ rad². Thus the finite range of the sampled frequencies includes the fraction

$$f_E \equiv \frac{\langle z^2 \rangle(N)}{\langle z^2 \rangle} = \frac{0.4219}{0.4296} = 0.982$$

of the total variance of the sea surface elevation. However, the corresponding fraction of the sampled slope variance is just $f_S = 0.02584/0.06011 = 0.430$. Thus $N = 1024$ is sampling 98% of the elevation variance but only 43% of the slope variance. This sampling is acceptable for creating a sea surface that looks realistic to the eye. However, the unsampled frequencies greater than the Nyquist frequency account for a large part of the optically important slope variance.

One way to account for the unsampled slope variance is to alias the variance of the waves with frequencies greater than the Nyquist frequency into the higher frequency waves with frequencies less than the Nyquist frequency. The higher frequency waves that are sampled will then contain too much variance, i.e., they will have amplitudes that are too large for their wavelengths, which will increase their slopes. This is done by adjusting or re-scaling the elevation spectrum

$$\tilde{\mathcal{S}}(k) \equiv [1 + \delta(k)]\mathcal{S}(k) \quad (8)$$

such that the integral of $k^2\tilde{\mathcal{S}}(k)$ over the sampled region k_f to k_{Ny} equals the integral of the true $k^2\mathcal{S}(k)$ over the entire spectral range. Sampling the re-scaled spectrum $\tilde{\mathcal{S}}(k)$ over the k_f to k_{Ny} frequency range then gives the same slope variance as would be obtained by sampling the true spectrum $\mathcal{S}(k)$ over the entire range of frequencies.

L is chosen so that the low frequencies are well sampled starting at the fundamental frequency k_f . There is thus no need to modify the low-frequency part of the variance spectrum, which if done, would adversely affect the total elevation variance. Only the high frequency part of the spectrum needs modification. A simple approach is to take $\delta(k)$ to be a linear function of k between the spectrum peak k_p and the highest sampled frequency k_{Ny} , and zero elsewhere:

$$\delta(k) \equiv \begin{cases} 0 & \text{if } k \leq k_p \\ \delta_{Ny} \left(\frac{k - k_p}{k_{Ny} - k_p} \right) & \text{if } k > k_p \end{cases} \quad (9)$$

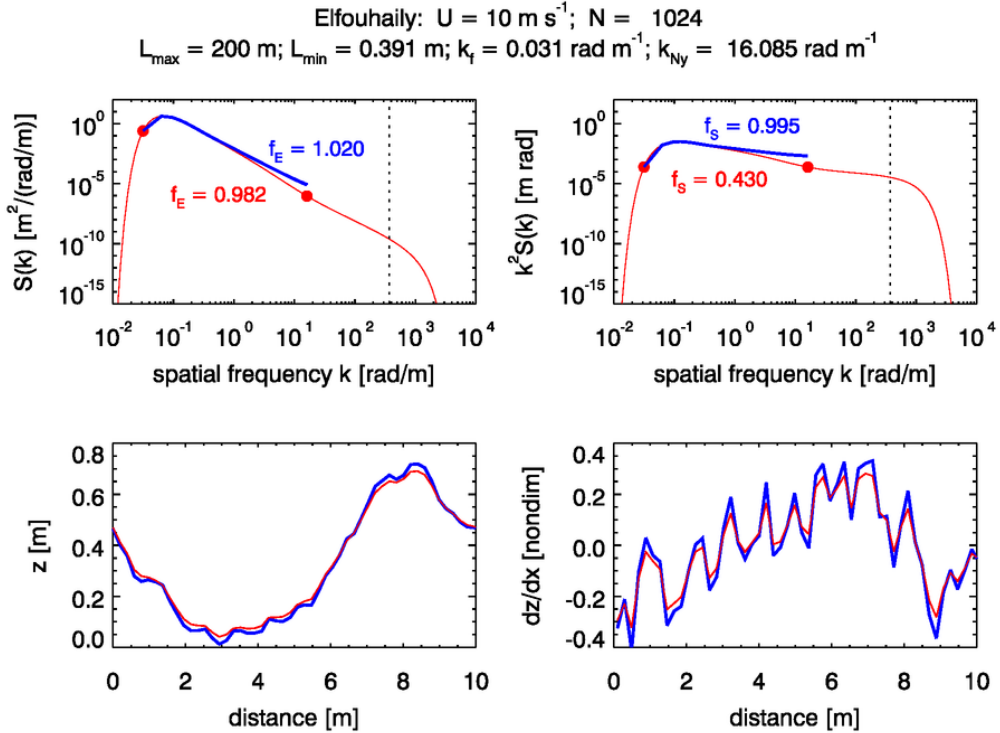


Fig. 1. (Color online) Example sampling of elevation and slope spectra. The red dots on the lines in the upper panels show the bounds of the elevation and slope spectra sampled using 1024 points with $L = 200$ m. The light red lines are the true spectra \mathcal{S} , and the truncated heavy blue lines are the adjusted spectra $\tilde{\mathcal{S}}$ obtained from Eqs. (8-10). The dashed lines at 370 rad/m indicate the conventional boundary between gravity and capillary waves. The lower panels show random realizations of short segments along the x direction of the sea surface elevation and slope for the true (light red line) and adjusted (heavy blue line) spectra.

δ_{Ny} is a parameter that depends on the spectrum (i.e., the wind speed), the size L of the spatial domain, and the number of samples N . δ_{Ny} must be determined so that $\delta(k)$ “adds back in” the unresolved slope variance. The added variance will be zero at the peak frequency k_p and largest at

the Nyquist frequency. That is, the $\delta(k)$ function will make only a small change to the variance spectrum at the low frequencies, and the change will be largest near the highest sampled frequencies, which is consistent with the idea that the high frequency waves have the largest slopes.

The parameter δ_{Ny} is determined by noting that

$$\begin{aligned} \sigma^2 &\approx \int_{k_0}^{k_\infty} k^2 \mathcal{S}(k) dk = \int_{k_0}^{k_{Ny}} k^2 \mathcal{S}(k) dk + \int_{k_{Ny}}^{k_\infty} k^2 \mathcal{S}(k) dk \\ &\equiv \int_{k_0}^{k_{Ny}} k^2 \tilde{\mathcal{S}}(k) dk = \int_{k_0}^{k_{Ny}} k^2 \mathcal{S}(k) dk + \delta_{Ny} \int_{k_p}^{k_{Ny}} k^2 \left(\frac{k - k_p}{k_{Ny} - k_p} \right) \mathcal{S}(k) dk. \end{aligned}$$

The right-most terms of these equations give (after

recalling that $\delta(k) = 0$ for $k \leq k_p$)

$$\delta_{Ny} = \frac{\int_{k_{Ny}}^{k_\infty} k^2 \mathcal{S}(k) dk}{\int_{k_p}^{k_{Ny}} k^2 \left(\frac{k - k_p}{k_{Ny} - k_p} \right) \mathcal{S}(k) dk}. \quad (10)$$

The heavy blue lines in the upper panels of Fig. 1 show the $\tilde{S}(k)$ and $k^2\tilde{S}(k)$ spectra for the present example. It is clear that the $\delta(k)$ function has added progressively more variance to the higher frequencies. The re-scaled variance spectrum does of course contain somewhat more variance over the sampled region than does the true spectrum. As the upper inset f_E value shows, this re-scaling has increased the fraction of sampled/true variance from 0.982 to 1.020. However, the upper f_S number in the upper-right panel shows that 99.5% of the slope variance is now being sampled, as opposed to just 43% for the true spectrum. Having slightly too much total elevation variance is a good tradeoff for being able to model the optically important slope statistics.

The lower-left panel of Fig. 1 shows a ten-meter slice along x of a random realization of the surfaces generated from these two spectra (with the same set of random numbers). The surface elevations $z(x_r)$ from the true spectrum (shown as the light red line) and the re-scaled spectrum (thick blue line) are almost indistinguishable at the scale of this figure. The lower-right panel shows the surface slopes computed from finite differences of the discrete surface heights. The Cox-Munk along-wind mean square slope given by Eq. (1a) compares well with the value of 0.032 obtained with the re-scaled spectrum. However, the value obtained from sampling the true spectrum is only 0.022, or 70% of the Cox-Munk value.

Thus the $\delta(k)$ correction to an elevation variance spectrum reproduces, to within a few percent of the theoretical values, both the surface elevation and slope statistics that would be obtained from the underlying true variance spectrum if it were sampled with enough points to fully resolve the elevation and slope variances.

The surface generation techniques of this section give sea surfaces that correctly reproduce both the elevation and slope statistics of a real sea surface corresponding to the chosen variance spectrum. Figure 2 shows an example of a 2D sea surface generated using these techniques. The along-wind, cross-wind, and total slope variances for this realization are in good agreement with the respective Cox-Munk values of 0.032, 0.019, and 0.054. The significant wave height of $H_{1/3} = 2.18$ m for this realization with $L_x = 100$ m is somewhat less than the theoretical value of $H_{1/3} \equiv 4\langle z^2 \rangle = 2.622$ m obtained by numerical integration of the elevation variance spectrum. However, increasing L_x to 400 m accounts for the very longest waves and gives

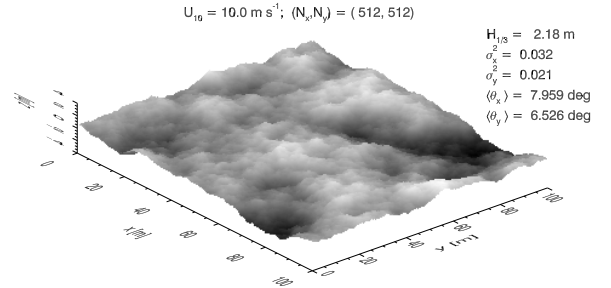


Fig. 2. Example 2D sea surface random realization for $L_x = L_y = 100$ m, $N_x = N_y = 512$, and a wind speed of 10 m s^{-1} . Light color is high surface elevation, dark color is low elevation. The inset numbers give the significant wave height $H_{1/3}$, slope variances in the along- and cross-wind directions, and mean surface tilt angles from the vertical.

$$H_{1/3} = 2.613 \text{ m.}$$

3. Polarized Ray Tracing

Ray tracing is most conveniently carried out if the surface is modeled as a grid of triangular wave facets. Resampling of rectangular FFT grids is described first. The process of ray tracing for polarized light is then outlined.

3.A. Resampling Rectangular Grids

The wave spectrum-FFT process gives sea surface elevations defined on a rectangular grid of points. The Monte Carlo computation of surface optical properties requires repeated determinations of the points of intersection of rays with surfaces, and of the angles of incidence of the rays with the surface normals at the points of intersection. Those calculations are most easily performed if the sea surface is modeled as a grid of triangular, rather than rectangular, wave facets. The mathematics then amounts to finding the intersection point of a line with a plane defined by the three vertices of a wave facet. The normal to the planar wave facet is easily computed from facet vertices.

If the FFT surface is generated using $N_y = N_x/2$, then essentially every other x grid point can be omitted to generate a hexagonal grid of triangular wave facets as illustrated in Fig. 3 for the case of $N_x = 16$ and $N_y = 8$ (and $L_x = L_y = 8$ m). This resampling generates $3(N_y/2)(N_y/2 + 1) + 1$ facet vertices and $3N_y^2/2$ wave facets. Although this resampling discards roughly half of the surface elevations computed by the FFT, the ray-tracing advantages obtained by the use of planar wave facets more than compensate for the extra FFT calcula-

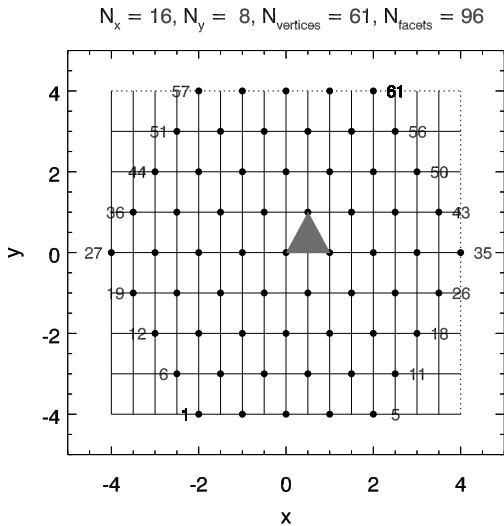


Fig. 3. Example mapping of a rectangular FFT grid (light lines) to a hexagonal grid of triangles as used in ray tracing. The dots show the triangle vertices. The FFT grid points at the right and top, shown by the dotted lines, are obtained by the inherent spatial periodicity of the surface as determined by FFT techniques. Thus the surface elevation of point 35 is the same as that of point 27, point 57 is the same as point 1, etc. One of the triangles generated from the FFT grid is shaded.

tions.

The Cox-Munk Eqs. (1) can be used to generate surfaces of triangular wave facets as described in [14, Section 4.3].

3.B. Ray Tracing

Tracing the path of a light ray through 3D space as it is reflected and refracted by the sea surface is in principle no more complicated than determining where a straight line intersects a plane. Those calculations are purely geometric and do not depend on the polarization state of the light. However, the application of the basic geometric concepts to the irregular geometry of the wave facets comprising a random realization of the sea surface is rather tedious. The details of those geometric calculations are given in [15, Appendix B].

Polarized light is described by the four-component Stokes vector $\underline{S} = [I, Q, U, V]^T$ whose Q and U components describe the state of linear polarization in a particular coordinate system. Incident rays approaching the sea surface before any interaction are described in a coordinate system based on the incident meridian plane, which is the plane containing the \mathbf{z} axis (outward normal to the

mean sea surface) and the direction ξ_i of the incident ray. The associated Stokes vector \underline{S}_i is specified relative to horizontal and vertical directions, \mathbf{h}_i and \mathbf{v}_i , which are respectively perpendicular and parallel to the incident meridian plane. Unit vectors \mathbf{h}_i and \mathbf{v}_i are determined so that “perpendicular” cross “parallel” is in the direction of light propagation. For an incident ray this rule gives

$$\mathbf{h}_i = \frac{\mathbf{z} \times \xi_i}{|\mathbf{z} \times \xi_i|}, \quad \mathbf{v}_i = \xi_i \times \mathbf{h}_i, \quad \xi_i = \mathbf{h}_i \times \mathbf{v}_i.$$

An incident ray always intersects a wave facet. The incident direction ξ_i and the wave facet normal \mathbf{n} define the scattering plane containing the incident, reflected (ξ_r) and transmitted (ξ_t) rays. The incident Stokes vector must be “rotated” (transformed) from the incident meridian plane into a coordinate system whose axes are perpendicular (\mathbf{s}) and parallel (\mathbf{p}) to the scattering plane. Using the choices of incident direction cross facet normal equals the perpendicular vector, and perpendicular cross parallel equals direction of propagation, gives

$$\mathbf{s} = \frac{\xi_i \times \mathbf{n}}{|\xi_i \times \mathbf{n}|} \quad \mathbf{p} = \xi_i \times \mathbf{s}, \quad \xi_i = \mathbf{s} \times \mathbf{p}.$$

Vector \mathbf{s} lies in the plane of the wave facet and is normal to each of ξ_i , \mathbf{n} , ξ_r , and ξ_t . Vector \mathbf{p} lies in the scattering plane and is normal only to ξ_i .

The rotation angle $0 \leq \alpha_i < 2\pi$ that rotates the incident Stokes vector into the scattering plane is the angle that rotates the initial perpendicular direction \mathbf{h}_i into the direction perpendicular to the scattering plane. (This same angle rotates \mathbf{v}_i into \mathbf{p} .) The rotation angle can therefore be obtained from the dot product of \mathbf{h}_i and \mathbf{p} . However, there is some ambiguity in the angle obtained this way. This is resolved by choosing a positive rotation to be counterclockwise when looking into the beam (in the $-\xi_i$ direction). In general, the rotation angle is the angle required to rotate the first vector \mathbf{v}_1 counterclockwise into the second vector \mathbf{v}_2 when looking into the rotation axis, which is vector $\mathbf{v}_3 = \mathbf{v}_1 \times \mathbf{v}_2$. In the present case, $\mathbf{v}_1 = \mathbf{h}_i$, $\mathbf{v}_2 = \mathbf{s}$, and $\mathbf{v}_3 = \xi_i$ is the rotation axis. In general, four cases must be considered, as shown in Fig. 4. The rotation angle depends on whether $\mathbf{v}_1 \cdot \mathbf{v}_2$ is positive or negative, and on whether $\mathbf{v}_1 \times \mathbf{v}_2$ is parallel or antiparallel to the rotation axis. In the present case, $\mathbf{v}_1 \times \mathbf{v}_2 = \mathbf{h}_i \times \mathbf{s}$ is by construction parallel to ξ_i , in which case

$$\alpha_i = |\cos^{-1}(\mathbf{v}_1 \cdot \mathbf{v}_2)| = |\cos^{-1}(\mathbf{h}_i \cdot \mathbf{s})|. \quad (11)$$

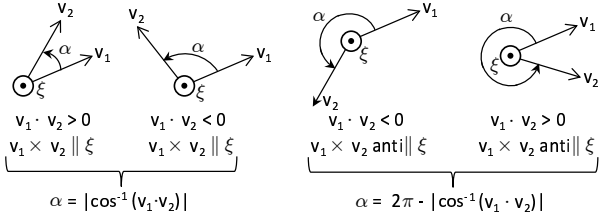


Fig. 4. The four cases for determining Stokes vector rotation angles. \mathbf{v}_1 is the initial direction, which is rotated into the final direction \mathbf{v}_2 by a counterclockwise rotation about direction ξ .

If $\mathbf{v}_1 \times \mathbf{v}_2$ is antiparallel to ξ , then

$$\alpha_i = 2\pi - |\cos^{-1}(\mathbf{v}_1 \cdot \mathbf{v}_2)| = 2\pi - |\cos^{-1}(\mathbf{h}_i \cdot \mathbf{s})|. \quad (12)$$

Vector $\mathbf{v}_1 \times \mathbf{v}_2$ is parallel (antiparallel) to ξ if the z component of $\mathbf{v}_1 \times \mathbf{v}_2$ has the same (different) sign as the z component of ξ .

Once the rotation angle has been determined, it is applied via a rotation matrix. For the choice of a positive rotation being counterclockwise when looking into the beam, the Stokes vector rotation matrix is [16, page 25]

$$\underline{R}(\alpha) = \begin{bmatrix} 1 & 0 & 0 & 0 \\ 0 & \cos 2\alpha & -\sin 2\alpha & 0 \\ 0 & \sin 2\alpha & \cos 2\alpha & 0 \\ 0 & 0 & 0 & 1 \end{bmatrix}.$$

Once a Stokes vector has been rotated into the local coordinate system of a wave facet, the 4×4 Fresnel reflection and transmission matrices are applied to obtain the reflected and transmitted (if any) Stokes vectors. There are four such Fresnel matrices, namely for reflection from the air side of a wave facet (denoted by matrix \underline{R}_{aw}), transmission from air to water (\underline{T}_{aw}), reflection from the water side of a facet (\underline{R}_{wa} , which may be total internal reflection), and transmission from water to air (\underline{T}_{wa}). These Fresnel matrices are given in [15, 17]. They depend only on the angle of incidence relative to the surface normal, $\theta_i = \cos^{-1}|\xi_i \cdot \mathbf{n}|$, and the index of refraction of the water.

When a ray eventually leaves the region of the sea surface, its final Stokes vector \underline{S}_f must be specified in the final meridian plane. The final horizontal and vertical directions are obtained from choosing the first direction to be the final ray direction $\xi_f (= \xi_r$ or $\xi_t)$ cross \mathbf{z} . Then, as above, $\mathbf{v}_f = \xi_f \times \mathbf{h}_f$. The final rotation angle α_f , which carries the Stokes vector from the most recent wave facet \mathbf{s} and \mathbf{p} axes to the final \mathbf{h}_f and \mathbf{v}_f axes, is obtained by Eq. (11) or (12).

A chain of one or more ray-surface interactions thus gives the final Stokes vector \underline{S}_f as

$$\begin{aligned} \underline{S}_f &= \underline{R}(\alpha_{m,f}) \underline{M}(\psi_m) \underline{R}(\alpha_{m-1,m}) \cdots \\ &\quad \underline{R}(\alpha_{1,2}) \underline{M}(\psi_1) \underline{R}(\alpha_{i,1}) \underline{S}_i \end{aligned} \quad (13a)$$

$$\underline{S}_f \equiv \underline{W}(\xi_i \rightarrow \xi_f) \underline{S}_i, \quad (13b)$$

where

- $\alpha_{i,1}$ is the rotation angle that rotates the initial \underline{S}_i into the scattering plane of the first wave facet.
- $\underline{M}(\psi_1)$ is any of the four Fresnel reflectance and transmittance matrices \underline{R}_{aw} , \underline{R}_{wa} , \underline{T}_{aw} , or \underline{T}_{wa} applied to the first ray-wave interaction.
- ψ_1 represents the scattering angle for the incident and reflected or transmitted directions used in the Fresnel matrix.
- $\underline{R}(\alpha_{1,2})$ is the rotation matrix that takes the Stokes vector $\underline{M}(\psi_1) \underline{R}(\alpha_i) \underline{S}_i$ from the scattering plane of the first wave facet to the scattering plane of the second wave facet.
- $\underline{R}(\alpha_{m-1,m})$ carries the current Stokes vector from wave facet $m-1$ to the last facet m .
- $\underline{M}(\psi_m)$ is the Fresnel reflection or transmission function for the last wave facet.
- $\underline{R}(\alpha_{m,f})$ is the rotation matrix that carries the Stokes vector from the scattering plane of the last wave facet to the final meridian plane associated with \underline{S}_f .

Note that only the incident and final Stokes vectors are referenced to a meridian plane.

Except for the case of total internal reflection of water-incident rays, each ray-surface interaction generates both a reflected and a transmitted ray. The information for each (point of intersection, direction, coordinate system, and weight) is stored in a stack array. The most recently stored ray is then selected for further processing. In this way, processing continues until all rays in the stack have been traced until they have left the surface region without further interaction and their final values have been tallied.

The continuous set of all directions is discretized by partitioning the directions into a set of rectangular (θ, ϕ) bins, plus two polar caps, which are collectively called quads. The quad partitioning used below has polar caps of five degree half angle and rectangular quads of $\Delta\theta \times \Delta\phi = 10 \times 15$ deg, except for $\Delta\theta = 5$ deg quads next to the equator of

each hemisphere. The same partitioning is used in the unpolarized HydroLight radiative transfer code. Rather than perform the ray tracing *de novo* for particular incident Stokes vectors, quad-averaged transfer matrices \underline{W} are computed for all pairs of quads. There are four sets of these transfer matrices, e.g., $\underline{W}_{\text{raw}}(Q_{ij} \rightarrow Q_{kl})$, which describes reflection for air-incident rays coming from quad Q_{ij} , corresponding to the i^{th} θ band and j^{th} ϕ band, and eventually being reflected upward after one or more ray-wave interactions into quad Q_{kl} . For particular quads Q_{ij} and Q_{kl} , $\underline{W}_{\text{raw}}(Q_{ij} \rightarrow Q_{kl})$ is thus a 4×4 scattering (Mueller) matrix that shows how any quad-averaged incident Stokes vectors $\underline{S}_i(Q_{ij})$ is transformed by reflection into a final Stokes vector $\underline{S}_f(Q_{kl})$. This matrix and its counterparts $\underline{W}_{\text{taw}}$, $\underline{W}_{\text{rwa}}$, and $\underline{W}_{\text{twa}}$ are optical properties of the sea surface itself and do not depend on the incident Stokes vector. Thus these matrices need be computed only once for a given wind speed (i.e., surface wave state) and water index of refraction.

The four sea-surface transfer matrices are statistically estimated as the ensemble averages of the transfer matrices computed for \mathfrak{S} independent surface realizations (\mathfrak{S} is typically of order 10^5). The calculation for a particular ray is initialized by setting \underline{W} to the 4×4 identity matrix. The random sequence of matrix multiplications seen in Eq. (13a) is then carried out. When a ray leaves the surface without further interaction, the current \underline{W} array is tallied to the accumulating array for the pair of quads containing the incident and final ray directions. For each sea surface realization, one ray is initialized from a random direction within each quad in the unit sphere of all directions. The averages of the \underline{W} arrays for the \mathfrak{S} surface realizations then yield the transfer matrices. Separate weight arrays are computed for singly and multiply scattered rays to enable quantification of the importance of multiple scattering.

The \underline{W} matrices computed in this manner are energy transfer matrices that give the fraction of energy in the incident quad that is reflected or transmitted into the final quad. These matrices can be converted to matrices for radiance reflectance and transmittance by incorporation of cosine and solid angle factors for the incident and final quads as shown in [14, Eq. (4.74)] and [15, Eq. (3.67)]:

$$\underline{R}(Q_{ij} \rightarrow Q_{kl}) = \underline{W}(Q_{ij} \rightarrow Q_{kl}) \frac{|\mu_i| \Omega_{ij}}{|\mu_k| \Omega_{kl}}. \quad (14)$$

Here μ is the average of $\cos \theta$ over the respective quad, and Ω is the solid angle of the quad. The

notation \underline{R} denotes a matrix for reflection or transmission of radiance, rather than for energy. For coherent incident Stokes vectors (in the sense of [16]) with units of irradiance (W m^{-2}), the final Stokes vector is obtained from $\underline{S}_f = \underline{W} \underline{S}_i$. If the incident Stokes vector is a diffuse vector [16] with units of radiance ($\text{W m}^{-2} \text{ sr}^{-1}$), then the radiance form is used: $\underline{S}_f = \underline{R} \underline{S}_i$. The radiance form is used if the transfer matrices are to be used as surface boundary conditions for solving the vector radiative transfer equation, e.g. as formulated in [15]. In either case, once the transfer matrices have been computed, any particular angular distribution of quad-averaged incident Stokes vectors can be transformed into reflected and transmitted Stokes vectors by simple matrix multiplications.

4. Sea Surface Reflectance and Transmittance

For an initial application of the above surface transfer functions, consider the easily understood case of an unpolarized, collimated source (e.g., the sun in a black sky). Figures 5-8 show the (temporally or spatially averaged) polarized reflectance and transmittance for a fully developed sea surface and a wind speed of 10 m s^{-1} . The surfaces were generated with FFTs using re-scaled variance spectra to fully resolve both elevation and slope variances. The sea surface region was $200 \times 200 \text{ m}$ with $N_x = 1024$ and $N_y = N_x/2 = 512$ as required for mapping the rectangular FFT grid to a hexagonal grid of triangular wave facets. Ray tracing was performed for 10^5 surface realizations (about 7 hours of computer time on a 2.4 GHz PC). The view is looking toward the point of reflection or transmission on the sea surface, i.e., looking at the glitter pattern, which is qualitatively shown by the size of the colored area. The source is thus located at the $\varphi = 180 \text{ deg}$ side the plotted hemisphere of directions, so the unscattered rays are traveling in the $\varphi = 0$ azimuthal direction. The incident Stokes vector in each case is unpolarized light, $\underline{S} = [1, 0, 0, 0]^T$. The incident direction is 50 deg from the zenith for air-incident light (Figs. 5 and 6) or 50 deg from the nadir for water incident light (Figs. 7 and 8). The upper left panel of each figure shows the percent of the incident energy that is reflected into each direction for quads of angular size $10 \times 15 \text{ deg}$ in polar and azimuthal angles. Quad boundaries are shown in gray, and the specular quad is outlined. Quads receiving less than 0.001% of the total energy are not colored. The asymmetry in φ is due to Monte Carlo noise in quads receiving almost no energy. The other panels show the degree of polarization of the reflected or transmitted light.

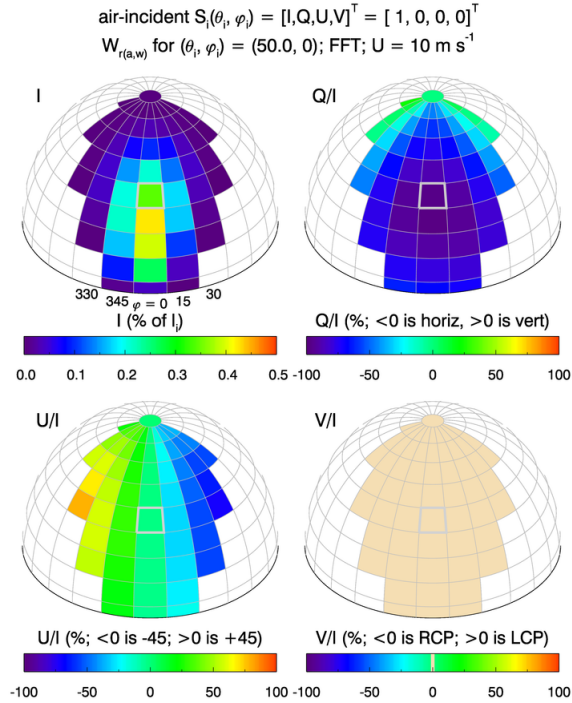


Fig. 5. (Color online) The reflected energy pattern (glitter pattern) for unpolarized air-incident light at a 50 deg incident angle from the zenith and a 10 m s^{-1} wind speed. The light source is in an otherwise black sky. The viewing direction is looking downward at the surface, facing the glitter pattern. The quad outlined in gray indicates the specular reflection quad that would receive all reflected light for a level surface. The tan color in the lower-right panel indicates values that are identically zero.

For the air-incident case of Fig. 5, 3.87% of the incident energy is reflected, and the remaining 96.13% is transmitted into the water. The upper right panel of Fig. 5 shows that the reflected light is as much as 97% horizontally polarized in the quads near $\theta = 50$ deg, which is near the Brewster angle of 53 deg for a level surface. The ± 45 deg polarization of the lower-left panel arises from rays being reflected by wave facets tilted to the left or right relative to the incident direction. Figure 6 shows the air-incident energy that is transmitted through the surface into the water.

Figures 7 and 8 show the corresponding results for water-incident unpolarized light, i.e., light incident onto the under side of the sea surface. Figure 7 shows the “underwater glitter pattern” as seen looking upward at the bottom of the sea surface. For this incident angle and wind speed, 60.42% of the incident energy is reflected back into the water. For a level surface, all of the energy would

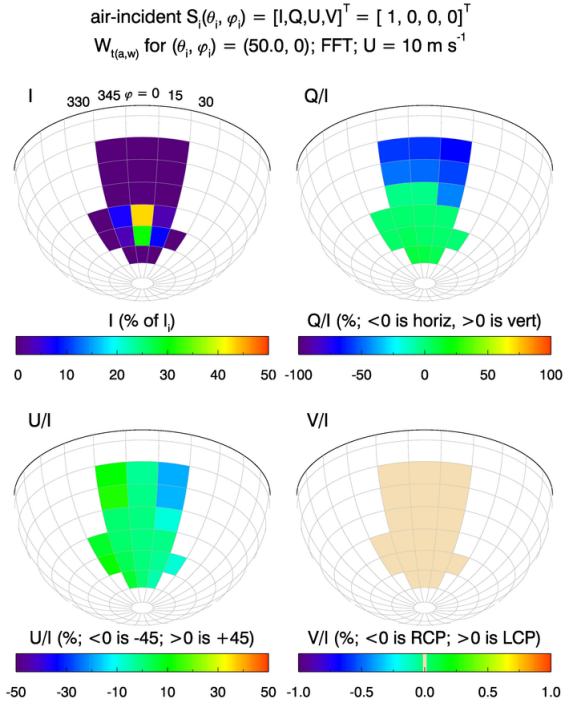


Fig. 6. (Color online) The transmitted energy pattern for air-incident light corresponding to Fig. 5. The viewing direction is looking upward at the surface from within the water.

be reflected because the incident angle of 50 deg is greater than the 48 deg critical angle for total internal reflection. For a wind-blown surface, some of the incident light intersects wave facets that are tilted so that the incident angle with the surface is less than the angle of total internal reflection, and 39.58% of the upwelling energy leaks through the surface into the air. In the upper right and lower left panels of Fig. 7, the large areas of unpolarized light near the horizontal (tan color) come from total internal reflection, which cannot change unpolarized incident light into any state of polarization.

It is easy to show that an arbitrary sequence of Fresnel reflection and transmission matrices and rotation matrices as seen in Eq. (13a) has the form

$$W = \begin{bmatrix} X & X & X & 0 \\ X & X & X & 0 \\ X & X & X & 0 \\ 0 & 0 & 0 & X \end{bmatrix},$$

where X denotes a non-zero value. (A specific example is given in Eq. (15) below.) Thus reflection and transmission of air-incident unpolarized or linearly polarized light cannot be converted to circular polarization. This is seen numerically in the lower right panels of Fig. 5 and 6, which show that the

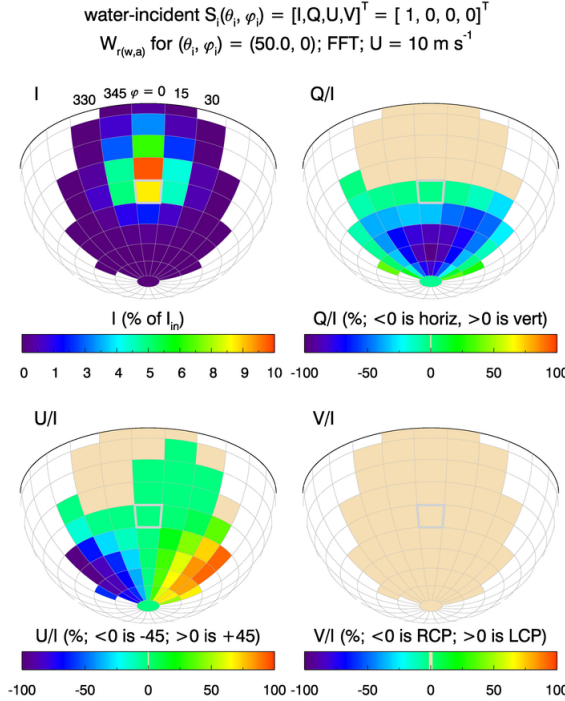


Fig. 7. (Color online) The reflected energy pattern (underwater glitter pattern) for water-incident light at a 50 deg incident angle from the nadir and a 10 m s^{-1} wind speed. The light source is unpolarized in an otherwise black ocean.

circular polarization is identically zero. However, total internal reflection leads to matrices of the form

$$W = \begin{bmatrix} X & X & X & 0 \\ X & X & X & X \\ X & X & X & X \\ 0 & X & X & X \end{bmatrix},$$

which still cannot convert unpolarized light into circular polarization. This seen numerically in the lower right panels of 7 and 8. However, if the incident upwelling underwater light is linearly polarized and undergoes total internal reflection, the reflected light can be circularly polarized. (This is of course the same physics used to generate circular polarization by total internal reflection in a Fresnel rhomb.) Total internal reflection is a potential source of elliptical or circular polarization in the ocean.

Figure 9 shows the percent of air-incident rays that undergo multiple interactions with surface wave facets. There is much more multiple scattering for Cox-Munk surfaces for incident angles between 30 and 70 deg, but more for the FFT surfaces at incident angles very near the horizon. The most common multiple-scatter event is one for which the incident ray is reflected into another wave facet, giving a final tally of one reflected and two refracted

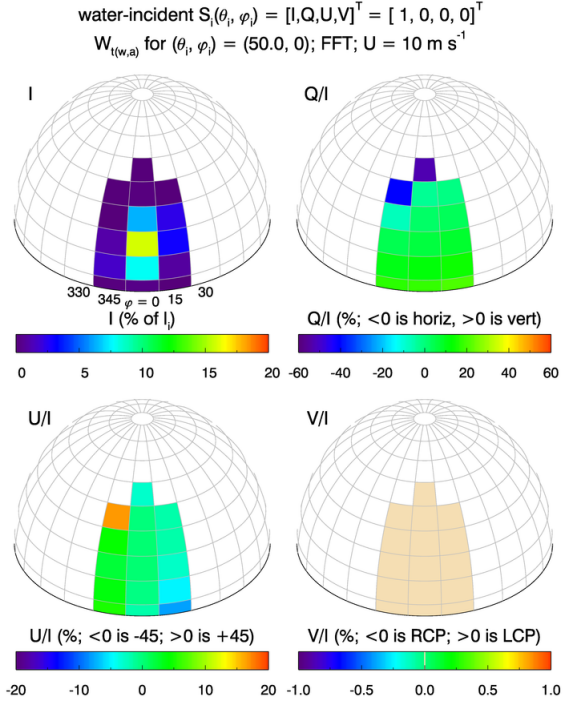


Fig. 8. (Color online) The transmitted energy pattern for water-incident light corresponding to Fig. 7. The viewing direction is looking downward at the surface from the air side.

rays. However, other combinations occur. For example, the incident ray may generate a reflected ray that leaves the surface without further interaction, and a refracted ray that intersects the surface again from the water side and undergoes total internal reflection. As with a single-scattering event, this multiple-scattering event gives a final tally of one reflected and one refracted ray. For large incident angles, rays occasionally have 10 or more interactions with the surface, but such events are rare—typically just one or two rays per ten thousand incident rays. The maximum number of multiply scattered rays is between 8 and 12% for Cox-Munk surfaces and 6 to 9% for FFT surfaces. The maximum occurs when the incident rays tend to be reflected into nearly horizontal directions, so that they are likely to intersect another wave. The dropoff for incident angles near the horizon occurs because those rays tend to intersect the sides of wave facets tilted toward the source such that the reflected ray heads upward, away from the surface.

5. Sea Surface Reflectance and Transmittance of Polarized Sky Radiance

Simulations as just seen using a collimated, unpolarized light source in an otherwise black sky or ocean are useful to illustrate the fundamental re-

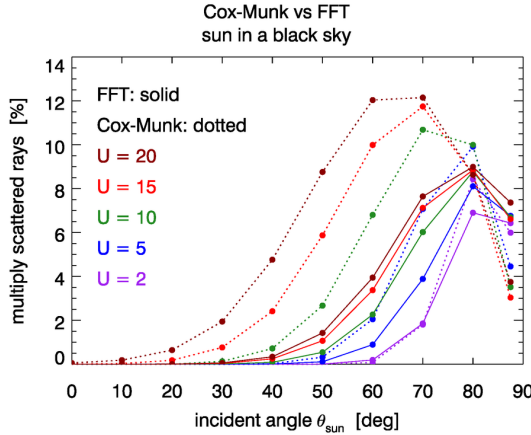


Fig. 9. (Color online) Percent of incident rays that undergo multiple interactions with the surface, as a function of wind speed and incident angle from the zenith, for FFT and Cox-Munk surfaces.

flection and transmission features of the sea surface. However, real skies are distributed light sources and are usually partially polarized.

The polarized sky radiance distribution is modeled as follows. Using water vapor, aerosol type, ozone concentration, and other conditions typical of a clear maritime atmosphere, the RADTRAN irradiance model [18] is run to obtain the direct (E_d^{dir}) and diffuse (E_d^{dif}) sky irradiances for the given solar zenith angle θ_{sun} and a wavelength of 550 nm. The quad containing the sun is given a radiance of magnitude $I_{\text{sun}} = E_d^{\text{dir}} / (\mu_{\text{sun}} \Omega_{\text{sun}})$, where μ_{sun} is the average of $\cos \theta$ over the sun's quad, and Ω_{sun} is the solid angle of this quad. The sun's direct beam is taken to be unpolarized: $\underline{S}_{\text{sun}} = [I_{\text{sun}}, 0, 0, 0]^T$. The angular pattern of the total radiance in the remaining quads is computed using the semi-empirical, clear-sky model of Harrison and Coombes [19]. Those diffuse sky radiances are scaled so that the total irradiance from the non-solar quad equals E_d^{dif} . This gives a calibrated sky $I(\theta, \phi)$ that reproduces the RADTRAN direct and diffuse irradiances. The polarization pattern of the diffuse sky radiance is that of a molecular (Rayleigh) single-scattering sky as given by the equations of Tilstra et al. [20]. Figure 10 shows, for a solar zenith angle of 50 deg, the resulting pattern of I and the degrees of total polarization $DoP = (Q^2 + U^2 + V^2)^{1/2} / I$, horizontal vs vertical (Q/I), and ± 45 deg (U/I) polarization. The circular polarization is identically zero. In the numerical calculations below, these equations are used to compute quad-averaged sky Stokes vectors.

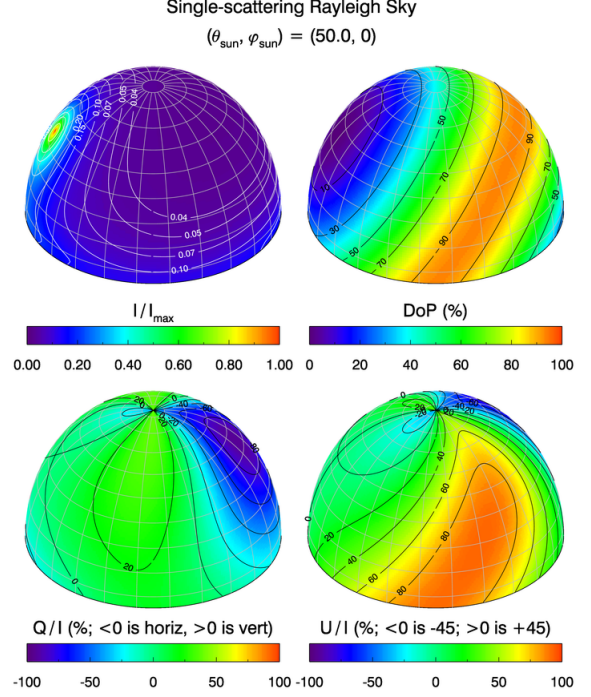


Fig. 10. (Color online) Sky radiance distribution for single-scattering by atmospheric molecules according to the Rayleigh scattering equations. The upper left panel shows the total radiance magnitude I relative to 1 in the sun's direction. The sun's location is at the left side of the plotted hemisphere of sky directions. The other panels show the degrees of total, horizontal vs vertical, and ± 45 deg polarization in percent.

Multiple scattering and aerosols tend to depolarize the sky radiance. Monte Carlo simulations of atmospheric radiance patterns [21] including molecular and aerosol components and multiple scattering show a similar polarization pattern but with the degree of polarization reduced by about 20%. Thus a polarization pattern corresponding to a single-scattering Rayleigh sky serves as an upper limit to the degree of polarization that occurs for a very clear atmosphere. Use of this sky radiance distribution in simulations thus gives an upper bound for the effects of polarization compared to simulations using unpolarized ray tracing.

Figure 11 is similar to Fig. 5 but shows the surface-reflected sky radiance for the sun at 50 deg and a polarized sky. The sea surface is an FFT surface for a wind speed of 10 m s⁻¹, generated with $L_x = 200$ m and $N_x = 1024$. For this sun zenith angle and atmospheric conditions, RADTRAN gives $E_d^{\text{dir}} = 0.6561$ and $E_d^{\text{dif}} = 0.3509$ W m⁻² nm⁻¹. The incident sky Stokes vectors are now diffuse vectors with units of spectral radiance, so the sur-

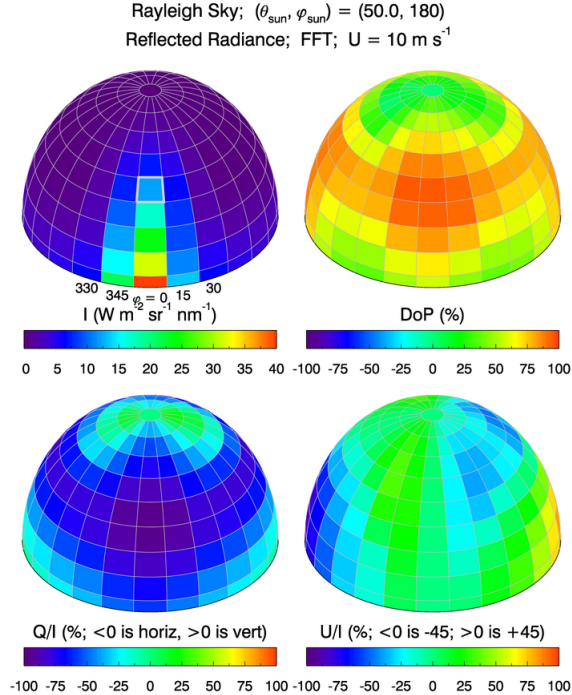


Fig. 11. (Color online) Surface-reflected radiance for a single-scattering Rayleigh sky and a wind speed of 10 m s^{-1} . The sun zenith angle is 50 deg and the viewing geometry corresponds to Fig. 5.

face reflectance function is an $\underline{R}_{\text{aw}}$ as defined in Eq. (14). All sky quads now in principle contribute to the reflected radiance in each quad:

$$\underline{S}_{\text{refl}}(Q_{kl}) = \sum_{ij} \underline{R}_{\text{aw}}(Q_{ij} \rightarrow Q_{kl}) \underline{S}_{\text{sky}}(Q_{ij}),$$

where the sum over ij indicates a sum over all sky quads.

Figure 12 shows the transmitted radiance corresponding to Fig. 11. As in Fig. 6, most of the transmitted radiance is concentrated into a few quads near the refracted direction of the sun's direct beam, and the radiance in those quads is only weakly polarized. However, the state of linear polarization away from the direct beam direction is determined by the sky polarization in directions away from the sun, and the degree of polarization can be large. However, those directions contain very little energy. For a level surface, all of the transmitted energy would be contained within the Snel's cone of angle 48.2 deg from the nadir. Now, however, for the 10 m s^{-1} wind speed, the rough surface allows radiance to be transmitted into all downwelling directions.

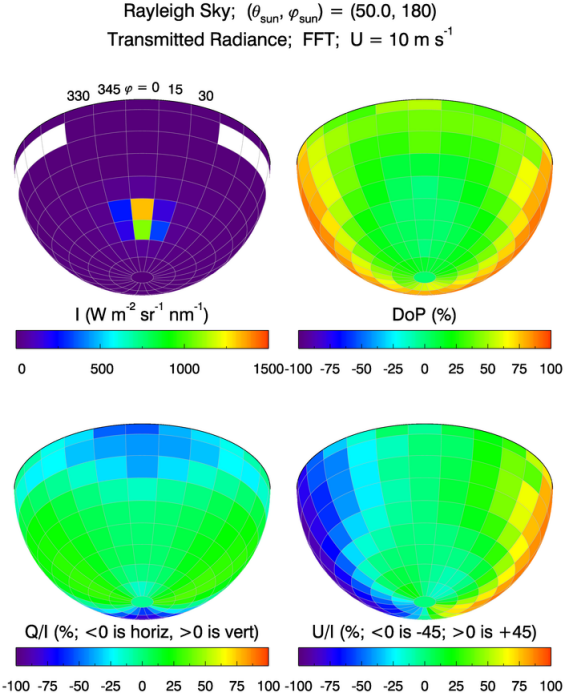


Fig. 12. (Color online) Surface-transmitted radiance for a single-scattering Rayleigh sky and a wind speed of 10 m s^{-1} . The sun zenith angle is 50 deg and the viewing geometry corresponds to Fig. 6.

6. Irradiance Reflectance

Surface irradiance reflectance is fundamental to energy transfer across the air-water surface. Although it is the total energy (without regard for the state of polarization) that is usually of interest, radiance reflectance by the surface depends on the state of polarization of the incident sky radiance, which in turn depends on the direction relative to the sun. Likewise, the reflectance depends on the angle between the incident radiance and the normal to the sea surface. It is therefore worthwhile to quantify the errors that may arise from the use of Cox-Munk surfaces and/or unpolarized ray tracing, compared to the more realistic FFT surfaces and polarized ray tracing.

The sky total downwelling plane irradiance is

$$E_d(\text{sky}) = \sum_{ij} I_{\text{sky}}(Q_{ij}) \mu_i \Omega_{ij}.$$

For the sky used to generate Fig. 11, $E_d(\text{sky}) = 1.0070 \text{ W m}^{-2} \text{ nm}^{-1}$, as expected from the input E_d^{dir} and E_d^{dif} values. The upwelling, surface-reflected irradiance computed from I_{refl} is $E_u(\text{refl}) = 0.05098 \text{ W m}^{-2} \text{ nm}^{-1}$. Thus, for the conditions of Fig. 11, $R_{\text{surf}} \equiv E_u(\text{refl})/E_d(\text{sky}) = 0.0506$. That is, about 5% of the incident energy is

reflected by the sea surface, and the remaining 95% enters the water column. It should be noted R_{surf} is the irradiance reflected of the surface itself, not the albedo of the water body. The albedo is defined in the same way, but the E_u includes both surface-reflected and water-leaving radiance. The albedo is therefore always somewhat greater than R_{surf} . For the 10^5 surface realizations used here, the statistical noise in R_{surf} is never more than 0.2%, and usually much less. This variability is too small to display on the curves of Fig. 13.

The upper left panel of Fig. 13 shows the dependence of R_{surf} on whether the ray tracing is polarized or unpolarized, for FFT surfaces and selected wind speeds. The polarized sky radiances were generated as described above for nominal solar zenith angles from 0 (the polar cap) to 87.5 deg (the quad next to the horizon). The corresponding first section of Table 1 shows the percent differences computed as $100[R_{\text{surf}}(\text{polarized}) - R_{\text{surf}}(\text{unpolarized})]/R_{\text{surf}}(\text{polarized})$. For the sun at the zenith, the difference in R_{surf} for polarized vs. unpolarized ray tracing is about 11%, i.e., polarized ray tracing gives a greater reflectance. For the near-horizon quad, the difference is -7.9% for a level surface to -11.7% for a wind speed of 15 m s^{-1} , i.e., polarized ray tracing gives somewhat less reflectance. The smooth line in this panel is the Fresnel reflectance for unpolarized light. This curve is valid only for uniform sky radiance distributions and a level sea surface. As seen here, for non-uniform skies and/or rough sea surfaces, the actual surface irradiance reflectance can be greater or less than the Fresnel reflectance. The decrease in irradiance reflectance for the sun very near the horizon has been explained previously [22]. In brief, as the sun goes from the zenith to the horizon, the fraction of diffuse sky irradiance increases from about 25% to over 99%. For solar zenith angles less than about 80 deg, the rapidly increasing Fresnel reflectance of the direct solar beam dominates and R_{surf} increases. But for sun zenith angles greater than 80 deg, diffuse radiance from directions nearer to the zenith dominates, and the lower Fresnel reflectance for those directions reduces R_{surf} . A lower fraction of the total radiance thus begins to enter the water as the sun nears the horizon, and R_{surf} decreases.

The upper right panel of Fig. 13 compares Cox-Munk and FFT surfaces for polarized ray tracing. The corresponding second section of Table 1 gives $100[R_{\text{surf}}(\text{FFT}) - R_{\text{surf}}(\text{Cox-Munk})]/R_{\text{surf}}(\text{FFT})$. Both surface models are of course identical for zero wind speed. There is very little difference in Cox-

Munk and FFT surfaces for solar angles less than about 50 deg. For wind speeds U less than about 10 m s^{-1} , the Cox-Munk surface has a greater R_{surf} at large solar zenith angles, and for wind speeds greater than 10 m s^{-1} , the reverse is true. The two surfaces give almost identical R_{surf} for all zenith angles when the wind speed is 10 m s^{-1} .

The middle left panel of this figure compares the commonly used unpolarized, Cox-Munk calculations with polarized, FFT computations. The corresponding section of Table 1 gives $100[R_{\text{surf}}(\text{FFT, pol}) - R_{\text{surf}}(\text{Cox-Munk, unpol})]/R_{\text{surf}}(\text{FFT, pol})$. The difference is greatest at large zenith angles, for which the unpolarized, Cox-Munk calculations give R_{surf} as much as 18% larger than the polarized, FFT calculations.

The above comparisons have included all orders of multiple scattering during the ray tracing. The middle right panel of Fig. 13 and the fourth section of Table 1 compare R_{surf} computed for multiple vs single scattering, for polarized ray tracing and FFT surfaces. The tabulated differences are now $100[R_{\text{surf}}(\text{multiple}) - R_{\text{surf}}(\text{single})]/R_{\text{surf}}(\text{multiple})$. Multiple scattering always gives a greater R_{surf} than single scattering, by about 2% to 8%, depending on the solar zenith angle and wind speed, with the greatest effect for nearly horizontal incident rays.

The preceding comparisons have been made with the sun at $\phi_{\text{sun}} = 0$, so that the sun's incoming rays are parallel to the wind. The lower left panel of 13 shows the results for FFT surfaces and polarized ray tracing when the sun is located at $\phi_{\text{sun}} = 90$ deg, for which the sun's incident rays are perpendicular to the wind speed. In this case, the surface reflectance is somewhat greater than for $\phi_{\text{sun}} = 0$. This is because the cross-wind wave slope variance is less than the along wind slope, as seen in Eq. (1b) vs Eq. (1a). Thus the incoming rays at right angles to the wind see a somewhat smoother sea surface, and the reflectance is consequently larger, than for rays incident in the along-wind direction.

The wave spectrum of [10] includes a parameter Ω_c that modifies the spectrum according to the age of the waves, that is, how long it has been since the wind began to blow. $\Omega_c = 5$ gives a very young sea for which the wind has been blowing only a short time and thus only capillary and small gravity waves are present. Ω_c decreases as the waves age and larger gravity waves develop. $\Omega_c = 1$ gives a mature sea, and $\Omega_c = 0.84$ gives the limiting steady state case of a fully developed

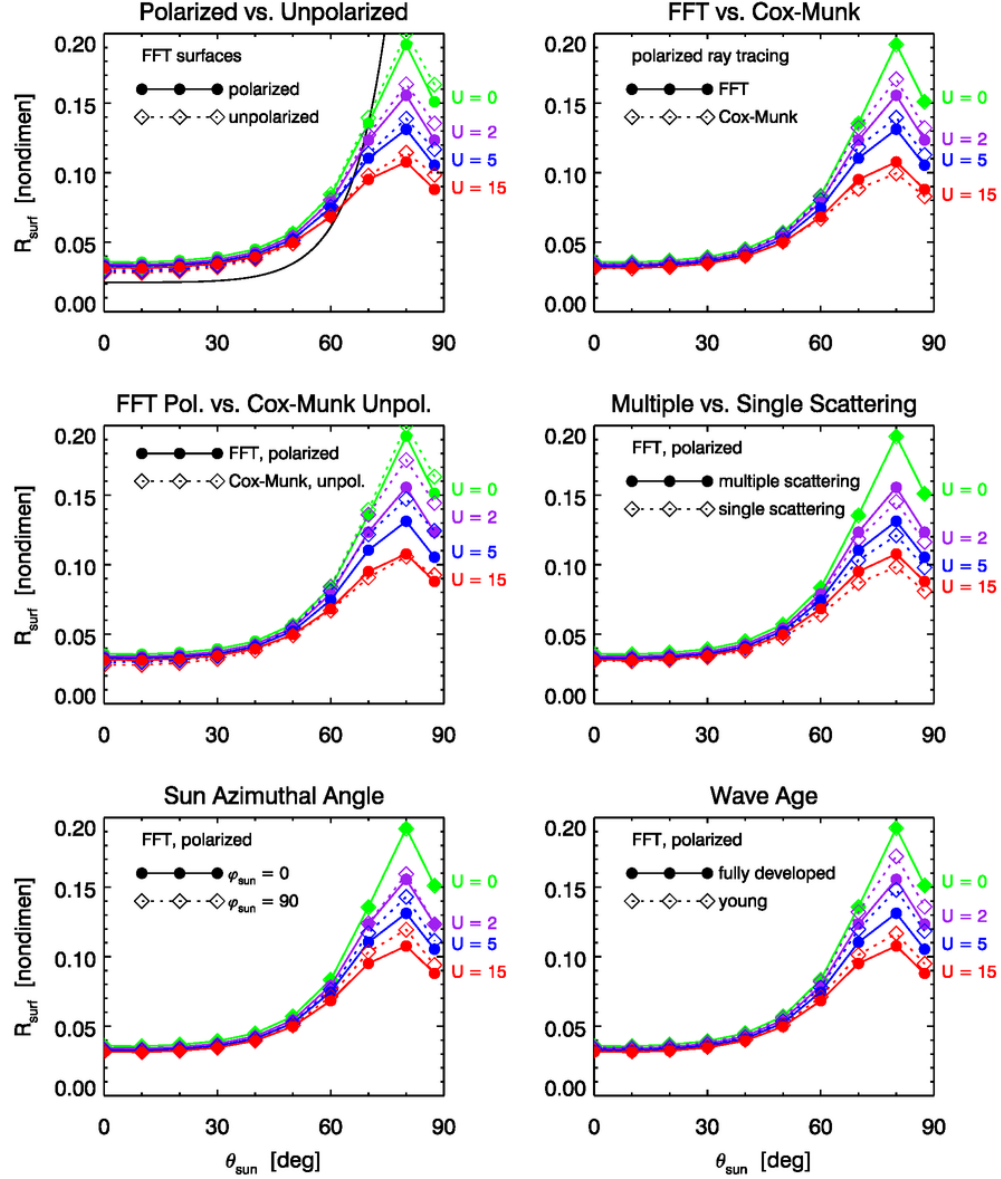


Fig. 13. (Color online) Comparison of surface irradiance reflectances R_{surf} as functions of solar zenith angle and wind speed for a polarized sky and various combinations of sea surface model (FFT vs. Cox-Munk), ray tracing (polarized vs. unpolarized), single vs. multiple scattering, sun azimuthal angle, and wave age.

sea. The lower right panel of the figure shows the effect of wave age for very young ($\Omega_c = 5$) vs. fully developed ($\Omega_c = 0.84$) seas, for FFT surfaces and polarized ray tracing (and $\phi_{\text{sun}} = 0$). The last section of Table 1 shows the corresponding percent differences $100[R_{\text{surf}}(\text{fully devel.}) - R_{\text{surf}}(\text{young})]/R_{\text{surf}}(\text{fully devel.})$. Young seas have a somewhat smoother surface, and thus a greater reflectance, because they have not had the time to

develop the slope variance that comes with a more mature sea.

In summary, the various approximations—Cox-Munk, unpolarized ray tracing, and single-scattering—and environmental conditions—sun azimuthal angle relative to the wind direction, and wave age—all give errors of order 10% in R_{surf} compared to the values computed with FFT surfaces and polarized ray tracing that includes all orders of

multiple scattering. However, as is clear from Fig. 13, these differences are considerably less than the systematic decrease in R_{surf} at large solar zenith angles due to wind speed. For zenith angles greater than 70 deg, R_{surf} decreases by about 30% when the wind increases from $U = 0$ to 5 m s $^{-1}$, and by almost 45% between $U = 0$ and $U = 15$ m s $^{-1}$. For solar angles less than 60 deg, R_{surf} decreases by 8% between $U = 0$ and 5 m s $^{-1}$, and by 12% between $U = 0$ and 15 m s $^{-1}$.

Table 1. Differences in surface irradiance reflectance R_{surf} as computed in various ways. The numbers are percent differences as defined in the discussion of Fig. 13.

U [m s $^{-1}$]	$\theta_{\text{sun}} = 0$	$\theta_{\text{sun}} = 87.5$
FFT: polarized vs. unpolarized		
0	+11.4	-7.9
2	+11.8	-9.8
5	+11.8	-10.8
10	+11.6	-11.4
15	+11.4	-11.7
polarized: FFT vs. Cox-Munk		
2	-2.0	-7.1
5	-2.3	-7.0
10	-0.6	-0.0
15	+1.1	+5.8
FFT polarized vs. Cox-Munk unpolarized		
2	+10.0	-17.0
5	+9.8	-18.0
10	+10.9	-11.2
15	+11.9	-5.1
FFT polarized: multiple vs. single scattering		
2	+1.7	+5.8
5	+2.2	+7.1
10	+2.5	+7.5
15	+2.7	+8.1
FFT polarized: sun azimuthal angle		
2	0.0	0.1
5	0.0	-5.7
10	0.0	-6.5
15	0.0	-6.9
FFT polarized: wave age		
2	-2.6	-10.2
5	-3.1	-12.4
10	-1.8	-6.3
15	-2.2	-8.0

7. Radiance Reflectance Factors

The remote-sensing reflectance R_{rs} is defined as the ratio of the water-leaving radiance L_w just above the sea surface to the downwelling plane irradiance E_d incident onto the sea surface: $R_{rs} \equiv L_w/E_d$. R_{rs} is the basis of most ocean-color remote sensing because this apparent optical property is strongly correlated with in-water optical properties and is minimally sensitive to environmental effects such as solar zenith angle, sky conditions, and wind speed [23]. However, any measurement of upwelling radiance L_u just above the surface includes both L_w and surface-reflected sky radiance L_{sr} , so that $L_w = L_u - L_{sr}$. For a level sea surface, L_{sr} comes only from sky radiance in the direction that is specularly reflected into the sensor. In this case $L_{sr}(\theta_v, \phi_v) = \rho(\theta_v, \phi_v)L_{\text{sky}}(\theta_v, \phi_v)$, where L_{sky} is the sky radiance and ρ is the radiance reflectance for the angle of incidence θ_v that connects L_{sky} and L_{sr} by specular reflection [24]. In $L_{sr}(\theta_v, \phi_v)$, θ_v is measured from the nadir; in $L_{\text{sky}}(\theta_v, \phi_v)$, θ_v is the same angle but measured from the zenith. For a level surface and unpolarized radiance, the radiance reflectance ρ equals the unpolarized Fresnel reflectance, which is a function only of θ_v .

For wind-blown sea surfaces, L_{sr} arises from sky radiance that is reflected by tilted wave facets from all sky directions into the sensor. However, for clear skies, it is still reasonable [9] to define a radiance reflection factor ρ that converts a sky measurement in a particular direction into an estimate of the surface reflectance: $\rho(\theta_v, \phi_v) \equiv L_{sr}(\theta_v, \phi_v)/L_{\text{sky}}(\theta_v, \phi_v)$. In this case ρ no longer equals the Fresnel reflectance, but rather depends on solar zenith angle, viewing direction, wave state, and sky condition. This ρ is best interpreted as a scale factor that converts a sky radiance measurement in a particular direction, $L_{\text{sky}}(\theta_v, \phi_v)$, into the surface reflectance in the corresponding specular direction, for given sky and sea surface conditions. The desired water-leaving radiance is then obtained from $L_w = L_u - \rho L_{\text{sky}}$. L_u and L_{sky} are measured by the same instrument, which is assumed to be insensitive to the state of polarization. Accurate determination of the value of ρ is the key to obtaining an accurate value for L_w .

Previous studies [9, 25] investigated the dependence of ρ on sun zenith angle, viewing direction, windspeed, and wavelength for clear sky conditions, and a table of ρ values is available [26]. These tabulated values are widely used [e.g. 27–29]. However, those values were computed using Cox-Munk surfaces and unpolarized ray tracing. The next section

re-evaluates ρ using FFT surfaces and polarized ray tracing.

7.A. ρ for a Level Sea Surface

Consider first the case of a level sea surface and a Rayleigh polarized sky radiance distribution as described above and illustrated in Fig. 10 for a solar zenith angle of $\theta_{\text{sun}} = 50$ deg. The left panel of Fig. 14 shows the reflectance factor for a level surface and unpolarized ray tracing. The values computed by Monte Carlo ray tracing lie along the curve for unpolarized Fresnel reflectance. The computed values do not depend on the azimuthal view-

ing direction ϕ_v , which is measured relative to the sun's azimuthal direction. That is, $\phi_v = 0$ corresponds to looking toward the sun, $\phi_v = 90$ deg is looking at right angles to the sun's incident rays, and $\phi_v = 180$ deg is looking away from the sun. The right panel shows $\rho(\theta_v, \phi_v)$ for azimuthal directions of $\phi_v = 90$ and 135 deg. Now, however, the ρ value depends on the azimuthal direction, even for a level sea surface. This ϕ_v dependence is easily understood as via a simple numerical example.

The surface radiance reflectance matrix as defined in Eq. (14) and computed by Monte Carlo simulation for incident and reflected angles $\theta_i = \theta_r = 40$ deg is

$$\underline{R}(40, \phi, 40, \phi) = \begin{bmatrix} 2.566 \times 10^{-2} & -1.963 \times 10^{-2} & 3.521 \times 10^{-7} & 0.0 \\ -1.963 \times 10^{-2} & 2.566 \times 10^{-2} & -7.489 \times 10^{-7} & 0.0 \\ 3.521 \times 10^{-7} & -7.489 \times 10^{-7} & -1.616 \times 10^{-2} & 0.0 \\ 0.0 & 0.0 & 0.0 & -1.616 \times 10^{-2} \end{bmatrix}. \quad (15)$$

This matrix is independent of azimuthal angle ϕ for a level sea surface. The Stokes vectors of the sky radiances in directions $(\theta_v, \phi_v) = (40, 90)$ and $(40, 135)$ are

$$\underline{S}_{\text{sky}}(40, 90) = \begin{bmatrix} 4.931 \times 10^{-2} \\ 2.403 \times 10^{-2} \\ 1.583 \times 10^{-2} \\ 0.0 \end{bmatrix}$$

and

$$\underline{S}_{\text{sky}}(40, 135) = \begin{bmatrix} 3.932 \times 10^{-2} \\ -1.418 \times 10^{-2} \\ 3.262 \times 10^{-2} \\ 0.0 \end{bmatrix}.$$

These sky radiances give $(DoP, Q/I, U/I) = (58.35, 32.10, 48.73)$ in percent for $(40, 90)$ and $(90.45, -36.06, 82.95)$ for $(40, 135)$, which match the values plotted at those directions in Fig. 10.

Multiplying $\underline{R}(40, \phi, 40, \phi)$ times these sky radiance Stokes vectors gives the corresponding surface-reflected radiances

$$\underline{S}_{\text{sr}}(40, 90) = \begin{bmatrix} 9.547 \times 10^{-4} \\ -5.617 \times 10^{-4} \\ -3.883 \times 10^{-4} \\ 0.0 \end{bmatrix}$$

and

$$\underline{S}_{\text{sr}}(40, 135) = \begin{bmatrix} 1.287 \times 10^{-3} \\ -1.136 \times 10^{-3} \\ -5.269 \times 10^{-4} \\ 0.0 \end{bmatrix}.$$

The corresponding ρ values are

$$\rho(40, 90) = \frac{I_{\text{sr}}}{I_{\text{sky}}} = \frac{9.547 \times 10^{-4}}{4.931 \times 10^{-2}} = 0.0194$$

$$\rho(40, 135) = \frac{I_{\text{sr}}}{I_{\text{sky}}} = \frac{1.287 \times 10^{-3}}{3.932 \times 10^{-2}} = 0.0327,$$

which are the values plotted for $\theta_v = 40$ in the right panel of Fig. 14.

For unpolarized ray tracing, only the $(1, 1)$ element of $\underline{R}(40, \phi, 40, \phi)$ is non-zero. In this case, for the same polarized sky radiances, the reflected radiances are

$$\underline{S}_{\text{sr}}(40, 90) = [1.265 \times 10^{-3}, 0, 0, 0]^T$$

and

$$\underline{S}_{\text{sr}}(40, 135) = [1.009 \times 10^{-3}, 0, 0, 0]^T$$

These values give

$$\rho(40, 90) = \frac{1.265 \times 10^{-3}}{4.931 \times 10^{-2}} = 0.0257$$

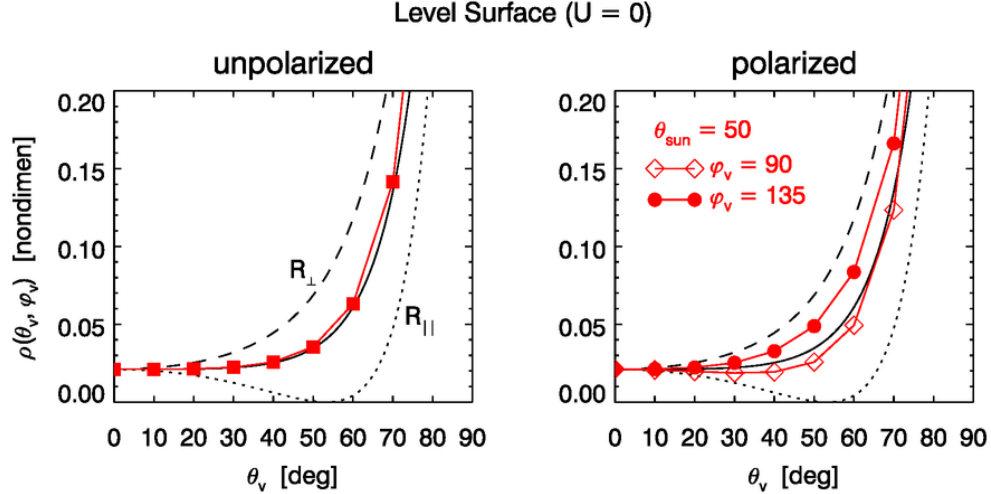


Fig. 14. (Color online) Radiance reflectance factors $\rho(\theta_v, \phi_v)$ for a level sea surface and a sun zenith angle of 50 deg. The left panel is for unpolarized ray tracing; the right panel is for polarized ray tracing. In both cases, the incident radiance is that of the single-scattering Rayleigh sky shown in Fig. 10. The dashed and dotted lines show the Fresnel reflectance for incident radiance that is linearly polarized perpendicular (R_{\perp}) or parallel (R_{\parallel}) to the incident meridian plane. The solid line without symbols is the Fresnel reflectance for unpolarized incident radiance.

and

$$\rho(40, 135) = \frac{1.009 \times 10^{-3}}{3.932 \times 10^{-2}} = 0.0257,$$

which are the values plotted in the left panel of Fig. 14.

Thus ρ is independent of azimuthal direction and the polarization state of the sky for unpolarized ray tracing. However, for polarized ray tracing, ρ depends on both polar and azimuthal angle even for a level sea surface because the state of the sky polarization is different for different directions. The polarization state of the incident radiance determines how much total radiance is reflected by the surface, hence the value of ρ . This is an additional complication in the determination of the value of ρ to be used in processing measured radiances. Not only does ρ depend on solar zenith angle, viewing direction, and sea state, it also depends on the state of polarization of the sky radiance distribution, even though the sensor itself is not sensitive to polarization.

7.B. ρ for Wind-blown Surfaces

Figure 15 shows for reference selected $\rho(\theta_v, \phi_v)$ values as computed by unpolarized ray tracing and Cox-Munk sea surfaces. ρ is shown as a function of off-nadir viewing direction θ_v for sun zenith angles of 30 and 60 deg, azimuthal viewing directions of 90 and 135 deg (relative to the sun at $\phi_v = 0$),

and wind speeds of 2, 5, 10, and 15 m s⁻¹. The plot for 10 m s⁻¹ reproduces the $\theta_{\text{sun}} = 30$ and 60 deg curves of [9, Fig. 6], but with less statistical noise because more rays are traced. When the sun is high in the sky (illustrated here by the $\theta_{\text{sun}} = 30$ curves) and the sea surface is rough (wind speeds of 5 m s⁻¹ or greater in the figure), the $\phi_v = 90$ curves have large ρ values at small θ_v values because of sun glint seen by the sensor measuring L_u . For large θ_v , ρ becomes large because of the rapidly increasing Fresnel reflectance. Based on plots such as these, [9] argued that $\theta_v = 30$ or 40 deg and $\phi_v = 135$ is a reasonable choice for field measurements. This viewing direction is a compromise that avoids most sun glint, keeps the instrument from looking at its own shadow, and gives minimal variability in the ρ values.

The solid-line curves in Fig. 16 show the corresponding values computed using FFT surfaces and polarized ray tracing. There is now a greater spread of ρ values for the given environmental conditions and viewing geometry. For $\theta_v = 40$ deg and wind speeds of 5 and 10 m s⁻¹, the unpolarized case gives tightly grouped values of $\rho = 0.0280-0.0285$ and $0.0316-0.0374$, respectively. However, the values determined by FFT surfaces and polarized ray tracing have a larger spread of values: $0.0179-0.0411$ for 5 m s⁻¹ and $0.0195-0.0458$ for 10 m s⁻¹. There is thus a factor-of-two spread in ρ values for each wind speed when computed with FFT surfaces and po-

larized ray tracing, vs. less than 20% spread when computed with Cox-Munk surfaces and unpolarized ray tracing. This figure also shows the curves for an azimuthal viewing direction of $\phi_v = 135$, but for the sun at a right angle to the wind speed, and for a very young sea ($\Omega_c = 5$ in the wave spectrum).

Figure 17 displays ρ values in two additional ways. The left panel shows a plot of $\rho(\theta_v, \phi_v)$ for a single sun angle of $\theta_{\text{sun}} = 40$ deg located at $\phi_v = 0$. The radial distance in the plot is the off-nadir viewing angle θ_v ; the center of the plot is looking straight down at the sea surface and the rim of the plot is looking towards the horizon. The sun's specular direction for a level surface is shown by the white quad centered at (40,0). The yellow to red colors in this area of the plot show the high ρ values needed to remove sun glint. The orange to red colors around the rim are high ρ values resulting from high Fresnel reflectances at large incident angles. The curves of Fig. 16 display the values from the center to the rim of the plot along the $\phi_v = 90$ and 135 deg directions (but for different sun zenith angles). The black dot at $\rho(\theta_v, \phi_v) = (40, 135)$ is the recommended viewing direction. In the present example, $\rho(40, 135) = 0.045$. The right panel of the figure shows $\rho(\theta_{\text{sun}}, \phi_v)$ for an off-nadir viewing direction of $\theta_v = 40$ deg. Now the center of the plot corresponds to the sun at the zenith, and the rim to the sun at the horizon. Again, the yellow-to-red colors show the high ρ resulting from sun glint with looking in directions too near the sun's azimuthal direction. The blue colors along $\phi_v = 135$ indicate ρ values in the 0.02 to 0.05 range for all sun zenith angles except when the sun is at the zenith or nearly so.

The simulations of this section used a wavelength of 550 nm for generation of the Rayleigh single-scattering sky radiance distribution. However, ρ also depends on wavelength [25] because the degree of sky polarization and the ratio of diffuse to direct solar irradiance vary considerably from blue to red wavelengths. Similarly, in a real atmosphere, the degree of sky polarization for a given wavelength is influenced by the aerosol type and optical thickness. However, Figs. 15 and 16 are sufficient to show that the previously computed ρ values based on Cox-Munk surfaces and unpolarized ray tracing [9, 26] are not adequate for accurate estimation of water-leaving radiance from above-surface measurements of upwelling and sky radiances. The viewing directions of $\theta_v \approx 40$ deg and $\phi_v \approx 135$ deg (relative to the sun's azimuthal direction) remain a reasonable choice. Harmel et al. [30] studied the

effects of polarization on a normalized reflectance, which is equivalent to the ρ of the present paper. Their study used an analytical representation of Cox-Munk surfaces with single scattering, but included atmospheric conditions for a range aerosol optical thicknesses. They, too, reached the same conclusion as the present study: it is imperative to account for polarization effects when estimating the amount of surface-reflected radiance in a measured total above-surface radiance.

Using the correct value of ρ is critical for the estimation of $L_w = L_u - \rho L_{\text{sky}}$ because the measured $L_{\text{sky}}(\theta_v, \phi_v)$ is typically an order of magnitude or more greater than L_w . Thus a small error in ρ can give a large error in L_w . To address the deficiency of the ρ values previously computed using Cox-Munk surfaces and unpolarized ray tracing, a new table of ρ values has been computed using FFT surfaces and polarized ray tracing. This table is available online [26].

8. Conclusions

Wave variance spectra and fast Fourier transforms are widely used in both science and the movie and video-gaming industries for the generation of random sea surfaces. The latter applications, especially, frequently ignore the scale factors needed to guarantee conservation of wave energy when going from variance spectra to sea surfaces. This paper has shown in Section 2 how the equations can be formulated to guarantee wave energy conservation. A new technique was presented in Section 2.C to account for both wave elevation and wave slope variances in generated sea surfaces, without the need for large numbers of spatial grid points. Random sea surface realizations were then used in Monte Carlo simulations of polarized ray tracing of air- and water-incident light. The ray-tracing algorithm outlined in Section 3.B follows each air- or water-incident ray through any number of ray-wave interactions, during which a single incident ray can generate any number of daughter rays by reflection and transmission. Electromagnetic energy is exactly conserved photon by photon because all incident and daughter rays are traced to completion when they leave the sea surface region to be tallied.

Sea surface energy reflection and transmission were first illustrated in Section 4 for the easily understood case of an unpolarized, collimated incident light source. Section 5 then illustrated reflection and transmission of polarized sky radiance. Section 6 studied the irradiance reflection properties of wind-blown sea surfaces. Irradiance reflectances R_{surf} computed using Cox-Munk wind speed-wave

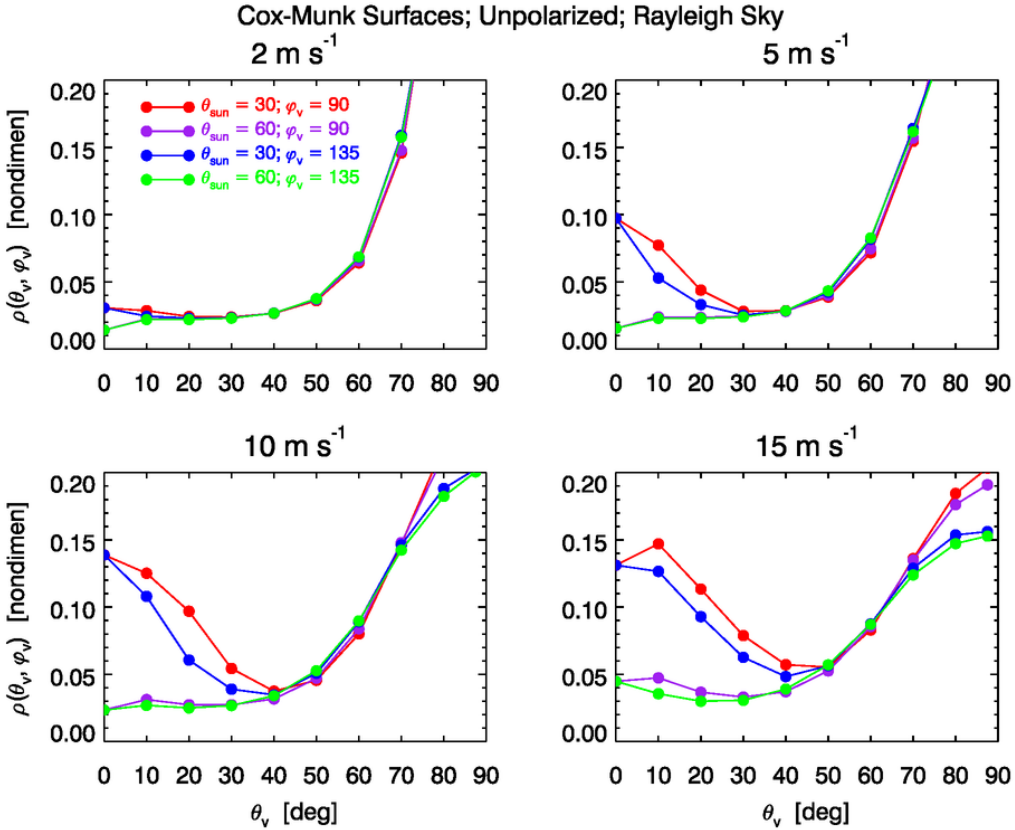


Fig. 15. (Color online) Radiance reflectance factors ρ computed using Cox-Munk surfaces and unpolarized ray tracing. The curves are for sun zenith angles $\theta_{\text{sun}} = 30$ and 60 deg, azimuthal viewing directions $\phi_v = 90$ and 135 deg, and wind speeds of 2 , 5 , 10 , and 15 m s^{-1} ; θ_v is the off-nadir viewing direction.

slope statistics and/or unpolarized ray tracing were compared with the values computed using FFT surfaces and/or polarized ray tracing. It was found (Fig. 13 and Table 1) that errors in R_{surf} due to ignoring polarization were typically greater than errors due to using Cox-Munk rather than FFT surfaces, or errors due to using single rather than multiple scattering. The differences between R_{surf} computed using Cox-Munk surfaces and unpolarized ray tracing, vs. FFT surfaces and polarized ray tracing, range from 10-12% for the sun at the zenith to as much as 18% for the sun near the horizon. This has implications for modeling of sea surface irradiance reflectance as needed for ecosystem models [22].

The last section studied radiance reflectance factors ρ , which are used in the estimation of water-leaving radiances from above-surface measurements of sky and upwelling radiances. These factors were shown to depend on the polarization state of the sky radiance distribution even though the measurements are made with sensors that are not sensi-

tive to polarization. Moreover, for a given viewing direction of the sensors, ρ as computed for FFT surfaces and polarized ray tracing was found to vary more with solar zenith angle and wind speed than the factors previously computed [9] using Cox-Munk surfaces and unpolarized ray tracing (Fig. 15 vs. 16). This result highlights the difficulty and importance of determining the correct value of ρ to use with particular environmental conditions of sun zenith angle and wind speed.

The author thanks Yogesh Agrawal for an enlightening discussion of wave spectra, which led to the algorithm of Section 2.C. The development of the surface generation and polarized ray tracing algorithms was supported by NASA contract NNH12CD06C. Publication of this paper was supported by NASA contract NNX14AQ49G.

References

- [1] C. Cox and W. Munk, “Measurement of the roughness of the sea surface from photographs of the sun’s glitter,” *J. Opt. Soc. Amer.* **44**, 838–850 (1954).

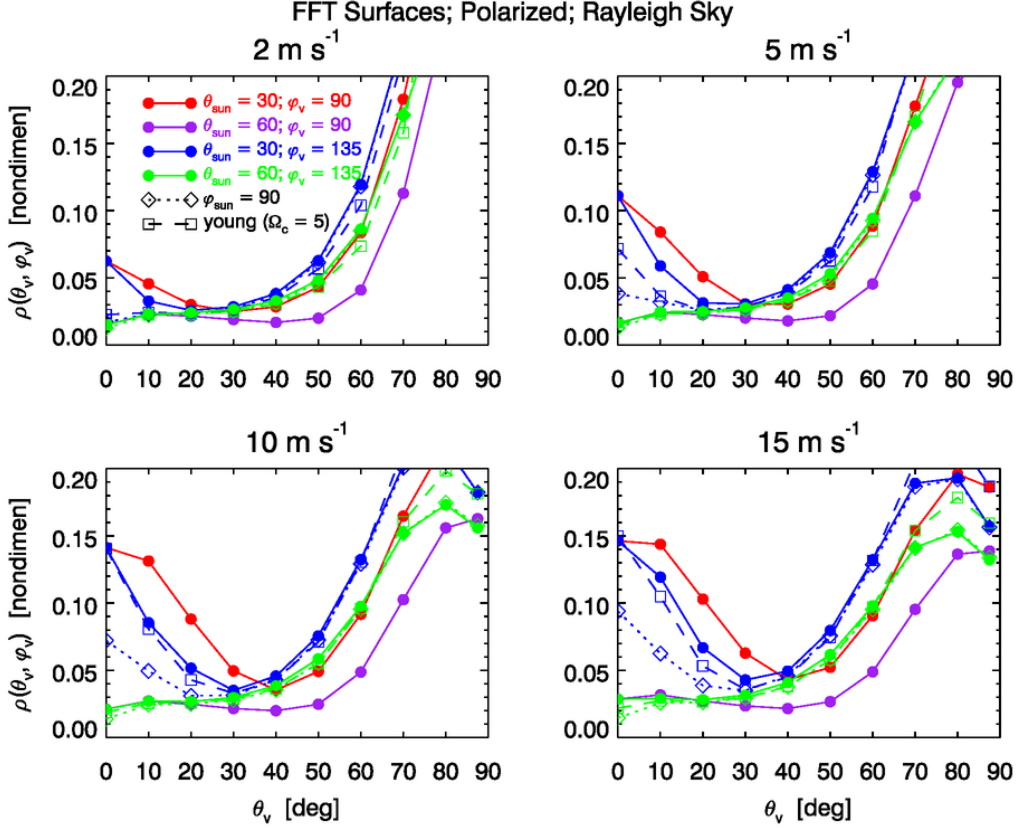


Fig. 16. (Color online) Radiance reflectance factors ρ computed using FFT surfaces and polarized ray tracing. The solid curves correspond to those of Fig. 15. These curves are for a fully developed sea and the sun's incident rays parallel to the wind speed ($\phi_{\text{sun}} = 0$). The dotted curves and diamond symbols show the curves for $\theta_{\text{sun}} = 30$ and 60 deg, azimuthal viewing direction of $\phi_v = 135$, but with the sun's azimuthal angle at $\phi_{\text{sun}} = 90$, so that the incoming rays are perpendicular to the wind direction. The dashed curves and box symbols show the curves for the $\theta_{\text{sun}} = 30$ and 60 deg, azimuthal viewing direction of $\phi_v = 135$, $\phi_{\text{sun}} = 0$, curves for a very young sea with $\Omega_c = 5$.

- [2] R. W. Preisendorfer and C. D. Mobley, "Albedos and glitter patterns of a wind-roughened sea surface," *J. Phy. Oceanogr.* **16**, 1293–1316 (1986).
- [3] M. P. Levesque and D. St-Germain, "Generation of synthetic IR sea images," in "SPIE Proceedings, vol. 1331, Characterization, Propagation, and Simulation of IR Scenes," (SPIE Optical Engineering Press, 1990), pp. 354–357.
- [4] M. P. Levesque, "Dynamic sea image generation," in "SPIE Proceedings, vol. 1486, Characterization, Propagation, and Simulation of IR Sources and Backgrounds," (SPIE Optical Engineering Press, 1991), pp. 294–300.
- [5] J. W. McLean, "Modeling of ocean wave effects for LIDAR remote sensing," in "SPIE Proceedings, vol. 1302, Ocean Optics X," (SPIE Optical Engineering Press, 1990), p. 480.
- [6] J. W. McLean and J. D. Freeman, "Effects of ocean waves on airborne lidar imaging," *Appl. Optics* **35**, 3261–3269 (1996).
- [7] S. Kay, J. Hedley, S. Lavender, and A. Nimmo-Smith, "Light transfer at the ocean surface modeled using high resolution sea surface realizations," *Optics Express* **19**, 6493–6504 (2011).
- [8] H. M. Tull Dahl and K. O. Steinvall, "Simulation of sea surface wave influence on small target detection with airborne laser depth sounding," *Appl. Optics* **42**, 000 (2004).
- [9] C. D. Mobley, "Estimation of the remote-sensing reflectance from above-surface measurements," *Appl. Optics* **38**, 7442–7455 (1999).
- [10] T. Elfouhaily, B. Chapron, K. Katsaros, and D. Vandemark, "A unified directional spectrum for long and short wind-driven waves," *J. Geophys. Res.* **102**, 15781–15796 (1997).
- [11] C. D. Mobley, "Modeling Sea Surfaces: A Tutorial on Fourier Transform Techniques," Tech. rep., Sequoia Scientific, Inc., Belle-

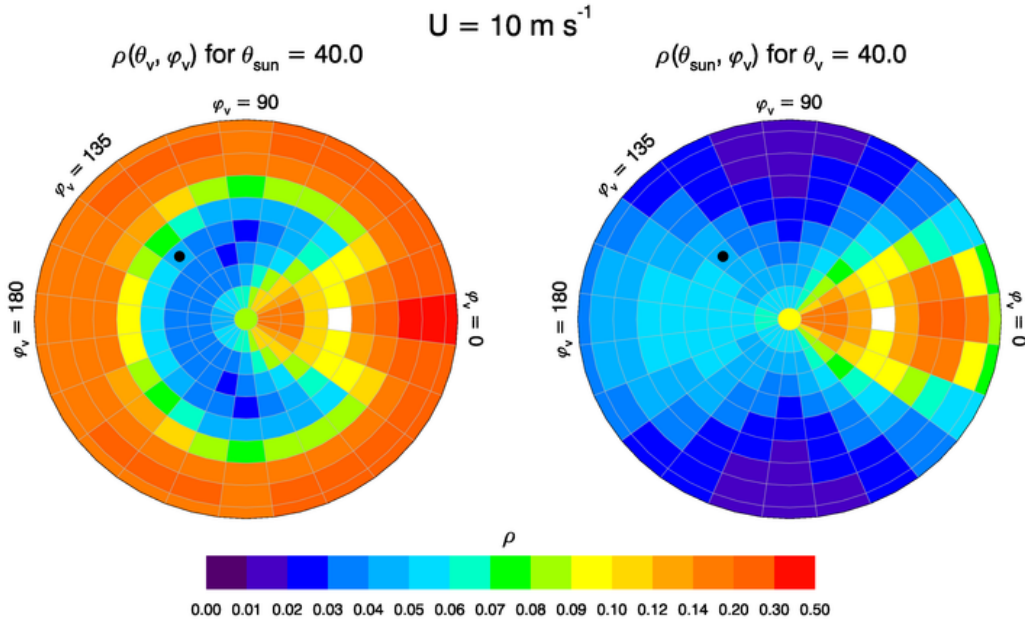


Fig. 17. (Color online) ρ for a wind speed of 10 m s^{-1} . The left panel shows ρ as a function of off-nadir and azimuthal viewing directions for a single sun angle of $\theta_{\text{sun}} = 40$ deg. The right panel shows ρ as a function of sun zenith angle and viewing azimuth for a fixed off-nadir viewing direction of $\theta_v = 40$ deg.

- vue, WA 98075 (2014). [Available online: www.oceanopticsbook.info/view/references/publications]
- [12] J. Tessendorf, “*Simulating Ocean Water*,” Tech. rep., SIGGRAPH Course Notes (2004).
 - [13] M. S. Longuet-Higgins, D. E. Cartwright, and N. D. Smith, “Observations of the directional spectrum of sea waves using the motions of a flotation buoy,” in “*Ocean Wave Spectra*,” (Prentice Hall, 1963), pp. 111–136.
 - [14] C. D. Mobley, *Light and Water: Radiative Transfer in Natural Waters* (Academic Press, 1994).
 - [15] C. D. Mobley, “*HydroPol Mathematical Documentation: Invariant Imbedding Theory for the Vector Radiative Transfer Equation*,” Tech. rep., Sequoia Scientific, Inc., Bellevue, WA 98075 (2014). [Available online: www.oceanopticsbook.info/view/overview_of_optical_oceanography/reflectances]
 - [16] M. I. Mishchenko, L. D. Travis, and A. A. Lacis, *Scattering, Absorption, and Emission of Light by Small Particles* (Cambridge Univ. Press, 2002).
 - [17] P.-W. Zhai, G. W. Kattawar, and Y. Hu, “Comment on the transmission matrix for a dielectric interface,” *J. Quant. Spectros. Rad. Trans.* **113**, 1981–1984 (2012).
 - [18] W. W. Gregg and K. L. Carder, “A simple spectral solar irradiance model for cloudless maritime atmospheres,” *Limnol. Oceanogr.* **35**, 1657–1675 (1990).
 - [19] A. W. Harrison and C. A. Coombes, “Angular distribution of clear sky short wavelength radiance,” *Solar Energy* **40**, 57–63 (1988).
 - [20] L. G. Tilstra, N. A. J. Schutgens, and P. Stammes, “*Analytical Calculation of Stokes Parameters Q and U of Atmospheric Radiation*,” Tech. rep., Koninklijk Nederlands Meteorologisch Instituut (KNMI), De Bilt, The Netherlands (2003).
 - [21] C. Emde, R. Buras, B. Mayer, and M. Blumthaler, “The impact of aerosols on polarized sky radiance: model development, validation, and applications,” *Atmos. Chem. Phys.* **10**, 383–396 (2010).
 - [22] C. D. Mobley and E. S. Boss, “Improved irradiances for use in ocean heating, primary production, and photo-oxidation calculations,” *Appl. Optics* **51**, 6549–6560 (2012).
 - [23] C. D. Mobley, “Reflectances,” http://www.oceanopticsbook.info/view/overview_of_optical_oceanography/reflectances (2010). [Online; accessed 27 January 2015].
 - [24] K. L. Carder and R. G. Steward, “A remote-sensing reflectance model of a red-tide dinoflagellate off West Florida,” *Limnol. Oceanogr.* **30**, 286–298 (1985).
 - [25] Z.-P. Lee, Y.-H. Ahn, C. D. Mobley, and R. Arnone, “Removal of surface-reflected light for the measurement of remote-sensing reflectance from an above-surface platform,” *Optics Express* **18**, 26313–26324 (2010).
 - [26] C. D. Mobley, “Surface reflectance factors,” <http://www.oceanopticsbook.info/>

- view/remote_sensing/level_3/surface_reflectance_factors (2013). [Online; accessed 27 January 2015].
- [27] S. B. Hooker, G. Zibordi, J. F. Berthon, and J. W. Brown, “Above-water radiometry in shallow coastal waters,” *Appl. Optics* **43**, 4254–4268 (2004).
- [28] G. Zibordi, B. N. Holben, I. Slutsker, D. Giles, D. D’Alimonte, F. Mélin, J. F. Berthon, D. Vandemark, H. Feng, G. Schuster, B. Fabbri, S. Kaitala, and J. Seppale, “AERONET-OC: A network for the validation of ocean color primary radiometric products,” *J. Atmos. Ocean. Technol.* **26**, 1634–1651 (2009).
- [29] T. Harmel, A. Gilerson, S. Hlaing, A. Tonizzo, T. Legbandt, A. Weidemann, R. Arnone, and S. Ahmed, “Long Island Sound Coastal Observatory: Assessment of above-water radiometric measurement uncertainties using collocated multi and hyperspectral systems,” *Appl. Optics* **50**, 5842–5860 (2011).
- [30] T. Harmel, A. Gilerson, A. Tonizzo, J. Chowdhary, A. Weidemann, R. Arnone, and S. Ahmed, “Polarization impacts on the water-leaving radiance retrieval from above-water radiometric measurements,” *Appl. Optics* **51**, 8324–8340 (2012).